APPLICATION OF FAST MARCHING METHOD

IN SHALE GAS RESERVOIR MODEL CALIBRATION

A Thesis

by

CHANGDONG YANG

Submitted to the Office of Graduate Studies of
Texas A&M University
in partial fulfillment of the requirements for the degree of

MASTER OF SCIENCE

Chair of Committee,	Akhil Datta-Gupta
Committee Members,	Michael King
	Yalchin Efendiev
Head of Department,	Dan Hill

August 2013

Major Subject: Petroleum Engineering

ABSTRACT

Unconventional reservoirs are typically characterized by very low permeabilities, and thus, the pressure depletion from a producing well may not propagate far from the well during the life of a development. Currently, two approaches are widely utilized to perform unconventional reservoir analysis: analytical techniques, including the decline curve analysis and the pressure/rate transient analysis, and numerical simulation. The numerical simulation can rigorously account for complex well geometry and reservoir heterogeneity but also is time consuming. In this thesis, we propose and apply an efficient technique, fast marching method (FMM), to analyze the shale gas reservoirs.

Our proposed approach stands midway between analytic techniques and numerical simulation. In contrast to analytical techniques, it takes into account complex well geometry and reservoir heterogeneity, and it is less time consuming compared to numerical simulation. The fast marching method can efficiently provide us with the solution of the pressure front propagation equation, which can be expressed as an Eikonal equation. Our approach is based on the generalization of the concept of depth of investigation. Its application to unconventional reservoirs can provide the understanding necessary to describe and optimize the interaction between complex multi-stage fractured wells, reservoir heterogeneity, drainage volumes, pressure depletion, and well rates. The proposed method allows rapid approximation of reservoir simulation results without resorting to detailed flow simulation, and also provides the time-evolution of the well drainage volume for visualization.

Calibration of reservoir models to match historical dynamic data is necessary to increase confidence in simulation models and also minimize risks in decision making. In this thesis, we propose an integrated workflow: applying the genetic algorithm (GA) to calibrate the model parameters, and utilizing the fast marching based approach for forward simulation. This workflow takes advantages of both the derivative free characteristics of GA and the speed of FMM. In addition, we also provide a novel approach to incorporate the micro-seismic events (if available) into our history matching workflow so as to further constrain and better calibrate our models.

DEDICATION

To my beloved parents for their selfless love and support.

To people around me to help me and share their lives with me.

ACKNOWLEDGEMENTS

First of all, I would like to express my gratitude to my academic advisor, Dr. Akhil Datta-Gupta, for his financial support academic guidance and encouragement throughout my master degree program.

I would like to thank my committee members, Dr. Michael King and Dr. Yalchin Efendiev, for their valuable comments and discussions.

I would like to thank Dr. Bin Gong and Dr. Dongxiao Zhang at Peking University for their recommendation for me to pursue studying in petroleum engineering at Texas A&M University.

I would also like to thank my senior student Jichao Yin, for his valuable research heritage, and senior student Jiang Xie, Yanbin Zhang, Han-Young Park for their constructive discussions, cooperation and suggestions in the completion of my research. Also thanks to the senior and current students, Song Du, Suksang Kang, Satyajit Taware, Jichao Han, Zheng Zhang, Jeong Min Kim, Shusei Tanaka, Shingo Watanabe, Dongjae Kam, Feyisayo Olalotiti-Lawal, Neha Bansal, Peerapong Ekkawong, Jixiang Huang, Xiaoyang Xia, Aditya Vyas, Yusuke Fujita, and other Chinese friends in our department, for their kind friendship, great inspiration and informative discussions.

TABLE OF CONTENTS

Page

LIST OF FIGURES

Page

Page

Page

LIST OF TABLES

Page

1. INTRODUCTION

1.1 Shale Gas Reservoir Development

Unconventional resources, such as shale gas, have taken a significant share of the U.S. energy supply and the world energy market (Holditch 2010). As suggested by Energy Information Administration (Fig.1), the shale gas will take up nearly half of the traditional energy supply by 2035. The growth of the development of these resources have been driven to a large extent by the advances in technologies such as horizontal well drilling and multistage hydraulic fracturing (Fig.2, Dong et al, 2013). To optimize the production of unconventional reservoirs, such as by bringing down costs, minimizing development risk, and increasing production, further technology advancement is needed as engineers today still face great challenges in understanding the fundamental mechanisms, from the pore scale to the field scale (Zhang et al. 2013). In order to reliably estimate unconventional reserves and ultimate recoveries, it is important to predict well performance accounting for the relevant reservoir and fracture parameters.

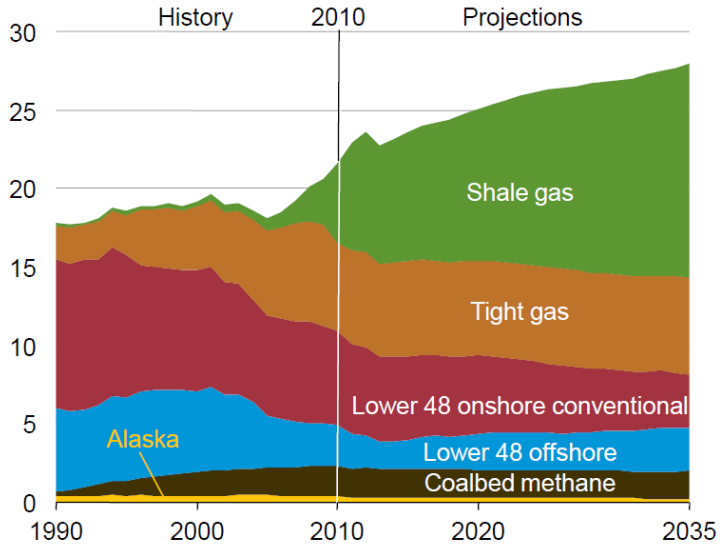

Fig.1 U.S. dry gas production (Tcf/year; EIA, Annual Energy Outlook 2012)

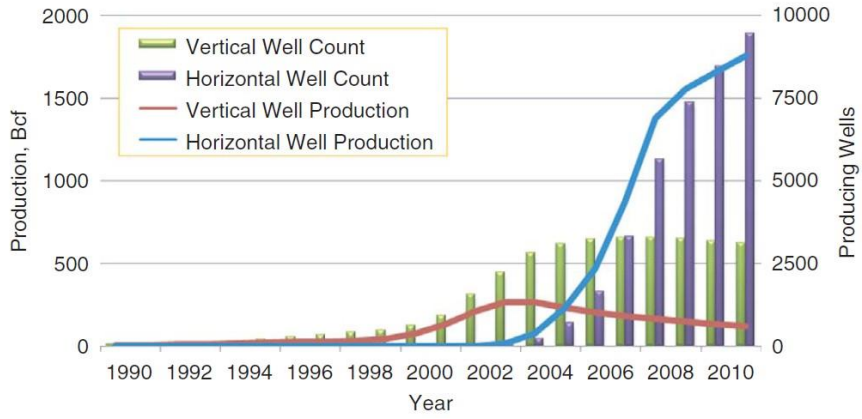

Fig.2 Production rapidly increased in the Barnett shale by horizontal wells

Currently, several types of analytical techniques are widely used for production forecasting in shale gas well development, including decline curve analysis (Fetkovich 1980; Valko and Lee 2010) and pressure/rate transient analysis (Ilk et al. 2010; Song et al. 2011; Clarkson et al. 2012). The methods in decline curve analysis largely involve curve-fitting, which is used to forecast production via extrapolation and obtain the estimated ultimate recovery (EUR). The experiences gathered by the engineer during the field development and the quantity and quality of completion and production data in a particular field heavily affect the predictive power. In pressure/rate transient analysis, reservoir and fracture parameters are first estimated by identifying flow regimes from simplified completion and reservoir models, and well production is predicted with the estimated properties. These two techniques are very useful, especially when limited subsurface information is available. However, analytical models become inadequate when we account for geometric complexity and reservoir heterogeneity through integration of geological, geophysical, and engineering data (Zhang et al. 2013).

In addition to the analytical methods, numerical simulation has also been utilized to perform unconventional reservoir analysis (Cipolla et al. 2009, 2011, 2012; Fan et al. 2010; Freeman et al. 2009). The advantage compared to analytical methods is that numerical simulation can rigorously account for complex fracture geometry, reservoir heterogeneity, reservoir compaction, and gas adsorption effects. (Zhang et al. 2013). However, numerical simulation can also be very time consuming, especially when high levels of grid refinements are used to accurately model complex fracture geometry, flow in the vicinity of the hydraulic fractures, and interaction with natural facture networks. Due to the high uncertainties associated with the development of unconventional reservoirs, it can be difficult and time consuming to calibrate such detailed numerical models using well performance data.

1.2 Fast Marching Method

In this thesis, we propose a novel approach for unconventional reservoir analysis based on the fast marching methods (Datta-Gupta et al. 2011; Xie et al. 2012a, 2012b; Zhang et al. 2013). This proposed approach can take more geometric complexity and reservoir heterogeneity into consideration compared to analytical methods; it can also help us understand the drainage process and well performance without involving detailed models and resorting to full numerical simulation. It stands midway between these two approaches, serving as a bridge for transition and a screening tool to select models when more and more data brought in during the development of a field.

Unconventional reservoirs are typically characterized by low permeabilities, and thus the pressure depletion from a producing well may not propagate far from the well during the

life of a development, i.e. the whole depletion process is in transient flow. The concept of depth of investigation can help us improve the understanding of unconventional reservoirs. We follow the definition of depth of investigation given by the "pressure front" propagation as proposed by Lee et al. (2003). The pressure front arrival time at a given point in the reservoir corresponds to the maximum in the derivative of the pressure response, i.e. the propagation of the peak pressure response corresponding to an impulse source or sink. The pressure front propagation equation turns out to be an Eikonal equation using a solution based on the high frequency asymptotic approach (Vasco et al. 2000). This Eikonal equation can be efficiently solved by the fast marching method (Sethian 1996, 1999; Xie et al. 2012a, 2012b).

The front propagation is determined in a single non-iterative calculation, which is extremely fast compared to a reservoir simulator. Only seconds are needed to simulate a million-cell model. The speed and computational efficiency of our proposed approach makes it ideally suited for parameter estimation and model calibration through inverse modeling of unconventional reservoir data. After spatially determining the pressure fronts, a pseudo-steady state pressure approximation within the moving front can be applied to approximate the pressure depletion and well performance (Xie et al. 2012b; Zhang et al. 2013). We can compute and visualize the time evolution of the well drainage volume and also estimated ultimate recovery (EUR).

1.3 Outline of the Thesis

The objectives of this thesis are threefold. In Chapter 2, we will first introduce the details of the concept of depth of investigation and describe how the fast marching method can be used to solve the pressure front propagation equation. Then, we will show the mathematical derivations for approximating the reservoir pressure depletion and well performance using a pseudo-steady state assumption. A simplified approach will be used to account for reservoir compaction effect. Drainage volume, stimulated reservoir volume and ultimate recovery can be approximated using the proposed method. In Chapter 3, a brief overview of automatic history matching methods will be given and details of genetic algorithm, one of the evolution methods, will be discussed. Using a synthetic multi-fracture reservoir model, the power of our method will be demonstrated using an integrated history matching workflow in Chapter 4. We also propose a novel method to integrate micro-seismic events into history matching workflow to better constrain the model. Micro-seismic data and production data are utilized to calibrate fracture/ matrix parameters for improved production forecast. Stimulated reservoir volume (SRV) is estimated using the calibrated models. Finally, we will present the major conclusions in the application of fast marching method to shale gas reservoir model calibration and also recommendations for future study.

2. FAST MARCHING METHOD: METHODOLOGY*

In this section, we discuss and derive the mathematical formulation of pressure front propagation equation based on the concept of depth of investigation. Then, we introduce a single-pass method, the fast marching method, to solve the Eikonal equation derived from the diffusivity equation. Based on a pseudo-steady state assumption, we can estimate the reservoir pressure behavior and well production rate using a geometric approximation. Also, the specific physical process associated with shale gas reservoir, for example, reservoir compaction effects, will be included in fast marching framework.

2.1 Depth of Investigation

Typical characteristic of shale gas reservoir is its extremely low permeabilities, and the pressure depletion from a producing well may not propagate far from the well during even the lifetime of the development. The boundary effects may never be seen, and all production is obtained during the transient flow regime. As a result, the concept of depth of investigation, and its application is now not just important for traditional well test analysis but also an important parameter to characterize the production of shale gas production wells.

We follow the definition of radius of investigation as given by the pressure 'front' propagation originally proposed by Lee (1982): the propagation distance of a 'peak' pressure disturbance for an impulse source or sink. For simplified flow geometries and

* Reprinted with permission from "Fast-Marching Methods for Complex Grids and Anisotropic Permeabilities: Application to Unconventional Reservoirs" by Zhang, Y., Yang, C., King, M.J., and Datta-Gupta, A. 2013. Paper SPE 163637 presented at SPE Reservoir Simulation Symposium, The Woodlands, Texas, 18-20 February. Copyright 2013 by SPE.

homogeneous reservoir condition, the radius of investigation can be calculated analytically. For 2D radial flow, the radius of investigation can be derived in field units as (Lee et al. 2003)

$$r = \sqrt{\frac{kt}{948\phi\mu c_t}} \qquad \text{Eq.1}$$

For different flow patterns, the analytical solution of radius of investigation can be generally written as follows:

$$r = \sqrt{\beta\alpha t} \qquad \text{Eq.2}$$

where r and t are propagation distance and time of the pressure front and α is the hydraulic diffusivity defined as $\alpha = k/(\phi\mu c_t)$. β is a geometric factor related to the flow patterns. For instance, for linear, radial, and spherical flow, β is 2, 4, and 6 respectively (Kim et al. 2009). However, the well-known formula in pressure transient analysis assume homogeneous reservoir properties, and are severely limited for heterogeneous and fractured reservoirs, particularly shale gas reservoirs with multistage fractures.

The Eikonal equation for the pressure front propagation is derived by Vasco et al. (2000) and Kulkarni et al. (2000). They introduced the concept of the diffusive time of flight using the asymptotic ray theory from geometric optics and seismology. Similar concept was developed earlier in the context of diffusive electromagnetic imaging by Virieux et al. (1994). By applying asymptotic expansion to the diffusivity equation, it can be shown that in the high frequency limit the pressure front propagation in an isotropic medium can be described by the Eikonal equation (detailed derivation of this diffusivity equation is sketched in Appendix A):

$$\sqrt{\alpha}\left|\nabla\tau(\vec{x})\right|=1 \qquad \text{Eq.3}$$

In this equation, the hydraulic diffusivity term $\alpha = k(\vec{x})/(\phi(\vec{x})\mu c_t)$ contains the reservoir heterogeneity information and is a function of space (can be a function of time also if we consider the time-dependent properties in shale gas reservoirs). Another unknown $\tau(\vec{x})$ is called the diffusive time of flight. Along a ray path, τ can be calculated from the following integral

$$\tau(r)=\int_0^r \frac{1}{\sqrt{\alpha}}dr' \qquad \text{Eq.4}$$

The ray path should satisfy Fermat's principle, which means that it is the one which minimizes the line integral of τ (Sun and Fomel 1998). For the purpose of characterizing the pressure front propagation, τ is conceptually a measure of distance rather than time and is analogous to the radius of investigation.

The diffusive time of flight τ is related to physical propagation time t of the pressure front through the following equation (Vasco et al. 2000; Kim et al. 2009):

$$\tau=\sqrt{\beta t} \text{ or } t=\tau^2/\beta \qquad \text{Eq.5}$$

Through the factor β, we can transform the entire diffusive time of flight field into a real pressure front arrival time field. By extending the radius of investigation through bringing in reservoir heterogeneity into the formula, we now lost the exact meaning of the factor β. In a heterogeneous case, there is no global flow pattern any more, and thus, β should be understood in an averaged sense and is related to the geometry of the

pressure front which can be of arbitrary shape and changing with time. Methods for calculating the factor β in heterogeneous case will be addressed later in Appendix C.

2.2 Efficient Method to Solve the Eikonal Equation: the Fast Marching Method

After deriving the pressure front propagation equation in the Eikonal equation form, the next step is how to solve this Eikonal equation efficiently. Instead of computing the diffusive time of flight by integrating along the pressure trajectories, we introduce a class of front tracking methods, called the Fast Marching Method (Sethian, 1999), to obtain the values of $\tau(\vec{x})$. It is a single-pass method which utilizes the fact $\tau(\vec{x})$ for the first-order PDE depends only on the value of τ along the characteristics passing through the point $\vec{x}$ (Sethian 1996). Thus, the solution of τ can be constructed in an orderly one-pass fashion from smaller values of τ to larger values. The basic framework for the fast marching method comprises the following steps (Sethian, 1999):

(1) Label all grid nodes as *unknown*;

(2) Assign τ values (usually zero) to the nodes corresponding to the initial position of the propagating front and label them as *accepted*;

(3) For each node that is *accepted*, locate its immediate neighboring nodes that are *unknown* and label them as *considered*;

(4) For each node labeled *considered*, update its τ value based on its *accepted* neighbors using the minimum of local solutions of Eq. (3) discussed later;

(5) Once all nodes labeled *considered* have been locally updated, we pick the node which has the minimum τ value among them and label it as *accepted*;

(6) Go to step (3) until all nodes are *accepted*.

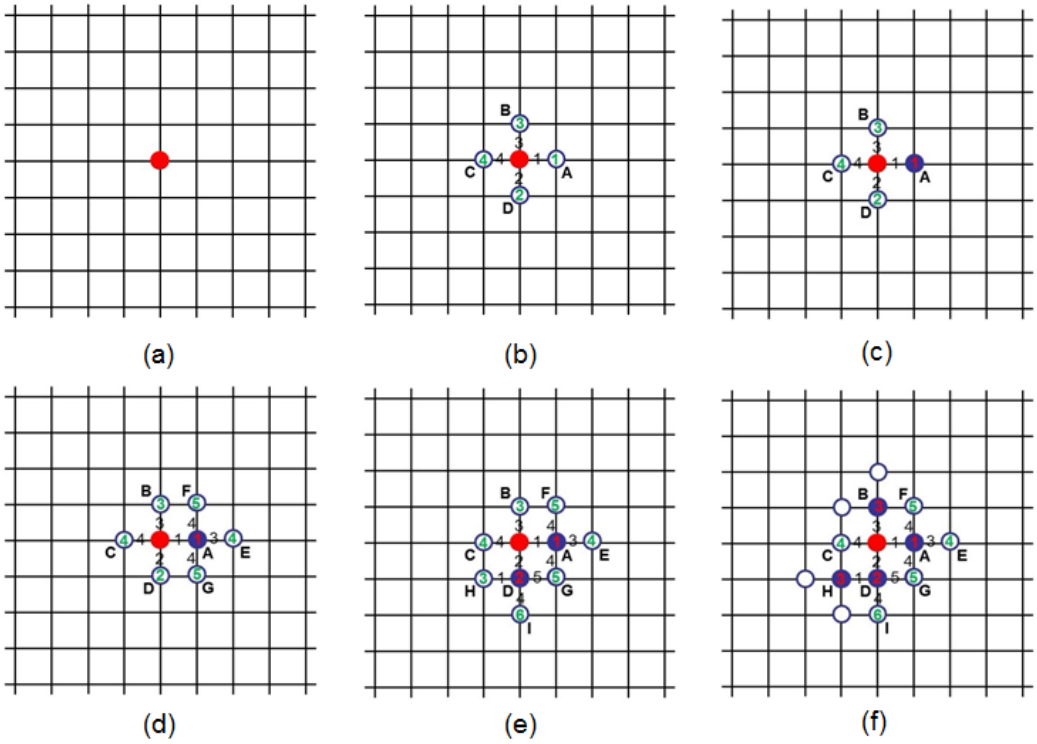

Fig.3 Illustration of FMM in 5-stencil Cartesian grid

In a 5-stencil Cartesian grid, these steps are illustrated in Fig. 3. We put the initial source point for the propagating front and label it as *accepted* (red solid) as shown in (a). Then its immediate neighbors A, B, C, and D are marked as *considered* (circle), and the diffusive time of flight τ it takes for the pressure front to arrive at these four points are updated as shown in (b). The numbers on the lines indicate the diffusive time of flight τ it takes for pressure to propagate between the two adjacent nodes and the numbers inside the circles are the cumulative τ for the pressure to propagate to these nodes from the source. We pick up the smallest one (point A in this case), and make it as *accepted* as show in (c). Then its neighbors E, G and F are added into the *considered* and the τ for them will be updated as shown in (d).These steps will repeat for the next

accepted point (like point D and then point H) as shown in (e) and (f). Basically, each time the new *accepted* point comes from the *considered* pool and has the smallest value of τ among all the *considered* points. If more than one point has the same smallest value of τ , we just accept them all at the same time. This process is repeated until the pressure front propagates the entire field.

For 5-stencil Cartesian grid, we can directly update the cumulative τ value by writing Eq.3 in a standard finite difference notation as (Sethian 1996):

$$\max\left(D_{ij}^{-x}\tau, -D_{ij}^{+x}\tau, 0\right)^2 + \max\left(D_{ij}^{-y}\tau, -D_{ij}^{+y}\tau, 0\right)^2 = \frac{1}{\alpha} \qquad \text{Eq.6}$$

Here the standard finite difference operator D for $\pm x$ directions can be written as $D_{ij}^{-x}\tau = (\tau_{i,j} - \tau_{i-1,j})/\Delta x$ and $D_{ij}^{+x}\tau = (\tau_{i+1,j} - \tau_{i,j})/\Delta x$. Similar equations hold for $\pm y$ directions. In Eq.6, τ values at *unknown* points are regarded as infinity and the "max" function is used to guarantee the "upwind" criteria. Eq. 6 leads to a quadratic equation and its minimum positive root gives us the τ value at point (i, j).

Alternatively, for a lattice we can calculate the τ values from each of the four quadrants (bottom-left, bottom-right, top-left, and top-right) and take the minimum τ value obtained. To locally calculate the diffusive time of flight it takes for front to propagate between two nodes, we can just use the ordinary finite differential form of Eq.3,

$$\delta\tau(\vec{x}) = \sqrt{\frac{\phi(\vec{x})\mu c_t}{k(\vec{x})}}\delta r \qquad \text{Eq.7}$$

Up to now, we can obtain a diffusive time of flight τ for each grid cell node. According to the relationship between τ and t in Eq.5, we can calculate the physical propagation

time t for each grid cell. Viewing from the arrival time map (or even directly from the diffusive time of flight map), we can obtain a very intuitive image about how fast each part of the reservoir can be drained. Fig.4 gives us the arrival time map for a 2-D homogeneous model for two scenarios. For the single vertical well case Fig.4 (a), the circular arrival time contour coincides quite well with analytical results (the black circle line). From the heterogeneous case, Fig.5, we show the fast marching method can accurately capture the high permeability trend.

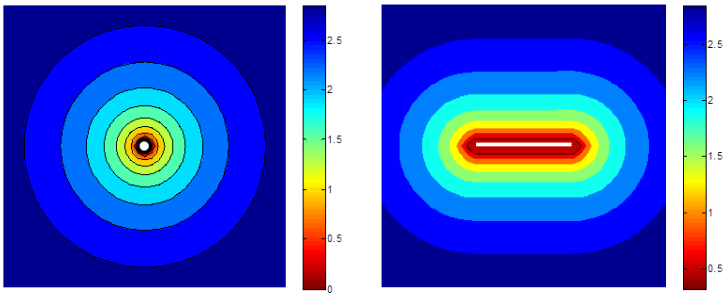

(a) (b)

Fig.4 Arrival time map for homogeneous case (days): a) vertical well;
b) vertical well with infinite-conductivity fracture

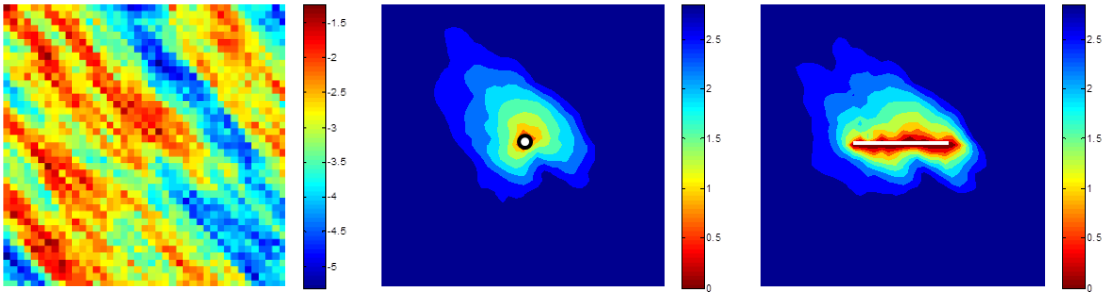

(a) (b) (c)

Fig.5 Arrival time map for heterogeneous case (days): a) permeability field (Log10 scale);
b) vertical well; c) vertical well with infinite-conductivity fracture

2.3 Drainage Volume Estimation

Just as discussed above, we can obtain the pressure front propagation arrival time at each grid by applying the fast marching method. When the pressure front arrives at that grid, it indicates that this grid is starting to be drained. In other words, all the mesh grids which have smaller arrival times (compared to the considered time) have already been drained. Therefore, the drainage volume at any time can easily be estimated by summing up the pore volumes of the mesh grids within that time contour.

Zhang et al (2013) have extended the fast marching method to unstructured grids and corner point grids. Thus, this kind of efficient drainage volume estimation method can be easily applied to very complex field scale reservoir models. For illustrative purposes, we show the results of drainage volume for a heterogeneous reservoir, shown in Fig.6, from Zhang et al (2013). The reservoir permeability field and hydraulic fracture geometry are shown in Fig.6 (a) and (b) respectively. The diffusive time of flight is calculated and shown in Fig.6 (c), which is then transformed into real arrival time. Fig. 6 (d) and (e) show the drainage volume at times 1 month and 30 years.

This time-evolution of drainage volume contains quite useful information about which part of the reservoir is drained very quickly and which part is left behind. One potential and very promising application of this technique is well placement optimization or hydraulic fracture optimization by optimizing the drainage volume for the economic lifetime of reservoirs. As the diffusive time of flight (or arrival time) can be calculated very efficiently using fast marching method, this technique is very suitable for this kind of optimization, even when large number of realizations are proposed.

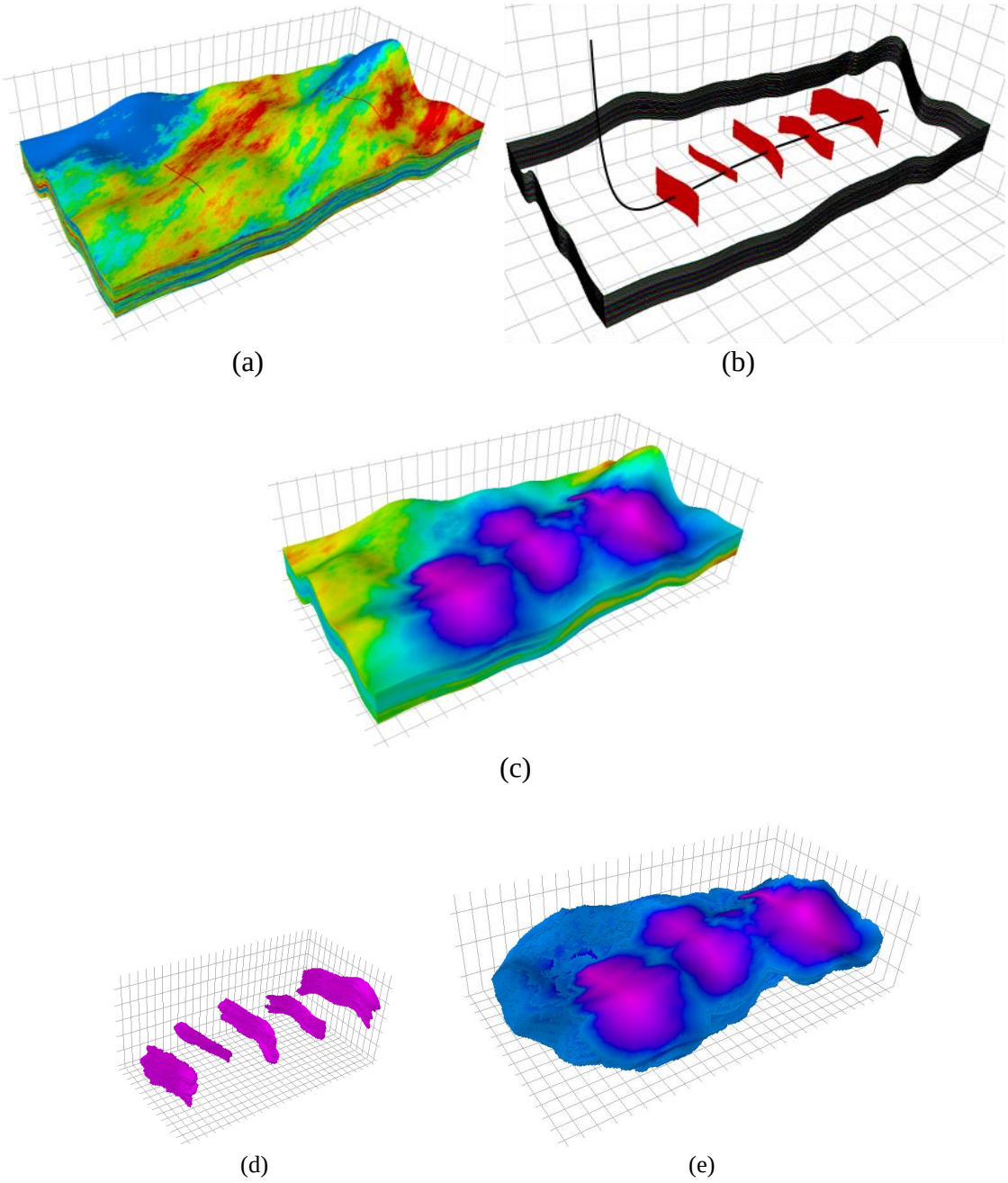

Fig.6 A synthetic example of a heterogeneous reservoir with five transverse hydraulic fractures: a) heterogeneous permeability field; b) the geometry of five transverse fractures; c) calculated diffusive time of flight map; d) drainage volume in 1 month; e) drainage volume in 30 years

Another application of the drainage volume calculation is to estimate the stimulated reservoir volume (SRV). For shale gas reservoirs, the production mainly comes from the

stimulated reservoir region because producing from the matrix will become very slow and might not be economical. Due to the characteristic that the permeabilities within the stimulated reservoir regions are generally higher than that of the matrix, the pressure front propagates much slower in the matrix compared to the stimulated reservoir regions. In particular, when we check the drainage volume evolution with time, we see the curve flattens out, which suggests the drainage volume has reached the boundary of the enhanced permeability zone.

We illustrate this idea with a single fracture from a multistage fractured horizontal well in an unconventional reservoir. In this example, the reservoir is characterized with three permeability regions: the effective fracture permeability, an enhanced permeability (10^{-2} to 10^{-3} md) region near the fracture and the matrix permeability (10^{-4} to 10^{-5} md) as shown in Fig.7 (a). From the arrival time of pressure front calculated using the fast marching method as shown in Fig.7(b), we can determine the drainage volume at different times, Fig.7(c). At approximately 100 days the curve flattens out which indicates that the drainage volume has reached the boundary of the enhanced permeability zone. The drainage volume at this time is essentially the pore volume corresponding to the stimulated reservoir volume (SRV). Subsequently, the drainage volume reaches the total reservoir pore volume as shown by the second plateau in Fig.7 (c), but only after orders of magnitude more time.

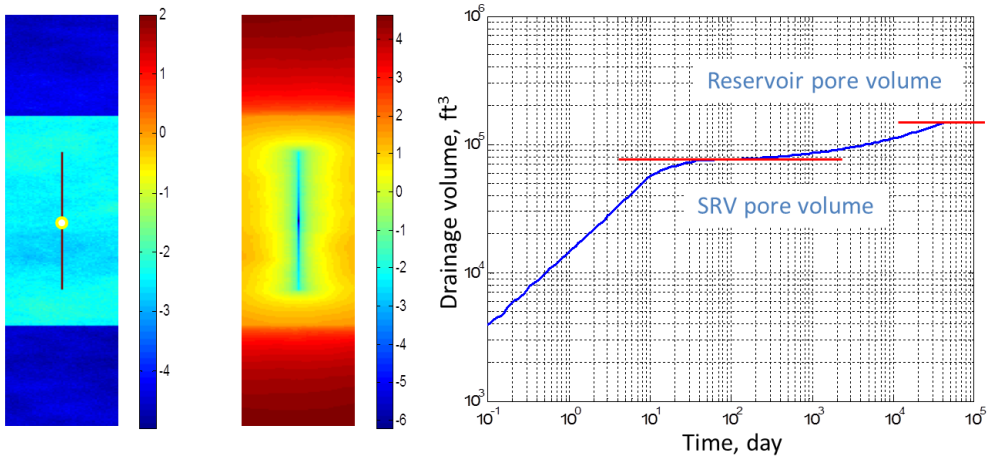

Fig.7 Top view of a single fracture from a multistage fractured horizontal well: a) permeability field; b) arrival time of pressure front; c) drainage volume versus time in log-log scale

2.4 Geometric Approximation Based on Drainage Volume Calculation

As discussed in previous section, the fast marching method is able to calculate the drainage volume V_p as a function of diffusive time of flight τ. According to the relationship between t and τ, we can easily obtain the drainage volume as a function of time, $V_p(t)$. Then a geometric approximation can be used to calculate the well production rate, and well bottom-hole pressure and average pressure within the drainage volume (Xie et al. 2012a, 2012b).

2.4.1 Geometric Pressure Approximation for Constant Rate Production

We start with expressing the diffusivity equation in terms of fluid flux for radially symmetric flow, given as

$$A(r)\cdot\phi\cdot c_t\frac{\partial p}{\partial t}=\frac{\partial q(r,t)}{\partial r} \qquad \text{Eq.8}$$

We use the change of variable,

$$dV_p=\phi\cdot A(r)\cdot dr \qquad \text{Eq.9}$$

and the chain rule

$$\frac{\partial}{\partial r} = \frac{\partial V_p}{\partial r}\frac{\partial}{\partial V_p} = \phi \cdot A(r)\frac{\partial}{\partial V_p} \qquad \text{Eq.10}$$

We can now express the diffusivity equation using the drainage volume as the spatial coordinate,

$$c_t \frac{\partial p}{\partial t} = \frac{\partial q(V_p, t)}{\partial V_p} \qquad \text{Eq.11}$$

The geometric approximation for the pressure solution is obtained from the following two approximations:

- The Darcy flux is negligible beyond the drainage volume, which means that the drainage volume acts as a moving no flow boundary.
- Within the drainage volume, the pressure is well approximated by a pseudo-steady state solution.

Then Eq.11, can be simplified as follows at well:

$$\frac{\partial p}{\partial t} \cong \frac{\partial \overline{p}}{\partial t} = -\frac{1}{c_t}\frac{q_{well}}{V_p(t)} \qquad \text{Eq.12}$$

The pressure drop within a small time increment can be obtained by

$$\delta p \cong \delta \overline{p} = -\frac{1}{c_t}\frac{q_{well}\delta t}{V_p(t)} \qquad \text{Eq.13}$$

2.4.2 Geometric Rate Approximation for a Constant Pressure Drop

We start with Darcy's law for radial flow,

$$q(r,t) = \frac{kA(r)}{\mu}\frac{\partial p(r,t)}{\partial r} \qquad \text{Eq.14}$$

Again, using a change of variable

$$dV_p = \phi \cdot A(r) \cdot dr \qquad \text{Eq.15}$$

and the chain rule

$$\frac{\partial}{\partial r} = \frac{\partial V_p}{\partial r}\frac{\partial}{\partial V_p} = \phi \cdot A(r)\frac{\partial}{\partial V_p} \qquad \text{Eq.16}$$

We can express the Darcy's law using the drainage volume as the spatial coordinate,

$$q(V_p,t) = \frac{k \cdot \phi \cdot A^2(V_p)}{\mu}\frac{\partial p(V_p,t)}{\partial V_p} \qquad \text{Eq.17}$$

Now, the pressure and Darcy flux are expressed in terms of drainage volume in the above equation. Permeability k is the averaged permeability over the surface area, A along the boundary of the drainage volume and so is the porosity ϕ. Notice that the drainage volume is considered as a new spatial variable in this formulation. We could have equivalently chosen to treat the diffusive time of flight τ as the spatial variable.

The Darcy flux in Eq.17 can be approximated as the production rate at the well location multiplied by a dimensionless flux along the drainage volume as follows (Winestock and Colpitts 1965),

$$q(V_p,t) = q_{well} \cdot q_D(V_p,t) \qquad \text{Eq.18}$$

Substituting Eq.18 into Eq.17, rearranging for pressure change and integrating with V,

$$\Delta p = p_i - p_{wf} = q_{well}(t) \cdot \mu \cdot \int_0^{V_p(t)} \frac{q_D(V,t)}{k \cdot \phi \cdot A^2} \cdot dV \qquad \text{Eq.19}$$

In principle, the integral should be taken till the boundary of the system. However, in practice, the dimensionless flux is sufficiently small beyond the depth of investigation,

and thus, this integral can be restricted over this finite moving boundary. As the well is being produced under a constant bottom hole flowing pressure, the pressure drop Δp can be considered to be specified, resulting in the calculation of the well rate.

We now make a few assumptions and observations to quantify the dimensionless flux, q_D in Eq.18 (Nordbotten et al. 2004),

1) Pseudo-steady state conditions exist inside the drainage volume. We can rewrite the diffusivity equation in terms of drainage volume just as in previous section,

$$c_t \frac{\partial p}{\partial t} = \frac{\partial q}{\partial V_p} = q_{well} \frac{\partial q_D(V_p)}{\partial V_p} \qquad \text{Eq.20}$$

Under pseudo-steady state, the left hand side of Eq.20 remains a constant. Thus the dimensionless flux q_D must be a linear function of drainage volume.

$$q_D(V_p) = a + b \cdot V_p \qquad \text{Eq.21}$$

2) Inner boundary Darcy flux, $q(0,t) = q_{well}$, which leads to $q_D(0) = 1$; Outer boundary Darcy flux $q(V_p, t) = 0$, which gives $q_D(V_p) = 0$.

With these assumptions, we can formulate the dimensionless flux as

$$q_D(V_p) = 1 - \frac{V_p}{V_p(t)} \qquad \text{Eq.22}$$

Substituting Eq.22 into Eq.19, rearranging equation to obtain expression for well rate,

$$q_{well}(t) = \frac{\Delta p}{\mu} \frac{1}{\int_0^{V_p(t)} \frac{1}{k \cdot \phi \cdot A^2} (1 - \frac{V_p}{V_p(t)}) \cdot dV_p} \qquad \text{Eq.23}$$

The production rate is in reservoir conditions; the oil or gas formation volume factor is needed to convert to standard conditions. In Eq.23, the integral can be approximated by finite summations shown as Eq.24. For convenience, we take the simulation time interval as discrete interval because the drainage volumes for previous time steps (step $1 \sim n-1$) are ready for time step n.

$$\int_0^{V_p(t)} \frac{1}{k \cdot \phi \cdot A^2}\left(1-\frac{V_p}{V_p(t)}\right) \cdot dV_p = \sum_{i=1}^{n}\left(\frac{1}{k \cdot \phi \cdot A^2}\right)_i \cdot \left(1-\frac{V_{p,i-1}}{V_p(t)}\right) \cdot \left(V_{p,i}-V_{p,i-1}\right) \qquad \text{Eq.24}$$

In Eq.24, the drainage volume $V_p(t)$ is calculated from the fast marching calculations corresponding to time step n. Taking the last term ($i = n$) in right hand side of Eq.24 as an example(i.e. considering the contribution of the shadowed red area sketched in Fig.8); the surface area A is the outer surface of the drainage volume $V_{p,n}$ (equals to $V_p(t)$) and can also be estimated during the drainage volume calculations. The permeability and porosity are arithmetically averaged properties within the shadowed red area and the incremental drainage volume is the shadowed red area, expressed as $dV_p = V_{p,n} - V_{p,n-1}$.

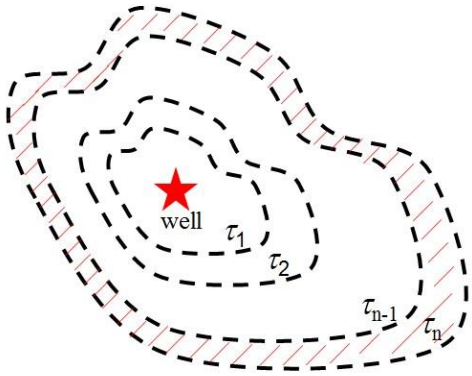

Fig.8 Illustration of calculating the integral with finite summation

In gas reservoirs, the gas viscosity and compressibility can be strongly dependent on the reservoir pressure. To account for these effects, pseudo-pressure and pseudo-time are commonly used in well test analysis (Lee et al. 2003). We just give the equation here and the details of the derivation can be found in the Appendix B.

$$q_g(t_p) = \frac{T_{sc}}{Tp_{sc}} \cdot \left(\frac{p}{\mu_g Z}\right)_i \cdot \frac{m(p_i) - m(p)}{\int_0^{V_p(t)} \frac{1}{k \cdot \phi \cdot A^2}\left(1 - \frac{V_p}{V_p(t_p)}\right) \cdot dV_p} \qquad \text{Eq.25}$$

Where pseudo-time t_p and pseudo-pressure $m(p)$ are defined as,

$$t_p = \left(\mu_g c_t\right)_i \int_0^t \frac{dt}{\mu_g c_t} \text{ and } m(p) = \left(\frac{\mu_g Z}{p}\right)_i \int_0^p \frac{pdp}{\mu_g Z} \qquad \text{Eq.26}$$

2.5 Reservoir Compaction Effect

For shale gas reservoirs, there are many complex physics involved, such as adsorption and desorption, Knudsen diffusion, and reservoir compaction (Javadpour et al. 2007). The reservoir compaction caused by pressure depletion can be quite significant and it would be desirable to incorporate this effect into the fast marching framework. We describe here a simplified approach to handle compaction effects and leave other complex physics for future exploration.

For pressure calculations using the geometric approximation, we use a series of time steps for the integration of Eq. 23. The pressure front location for each time is given by the fast marching solution with the original reservoir properties without compaction. This is because physically the pressure front should propagate monotonically outwards and will not move backwards. Therefore, we assume that the pressure fronts are the same with and without the compaction effects. However, in the presence of compaction,

the pressure drop Δp during the time interval Δt should be calculated using an effective drainage volume $V_{p,eff}(t)$ instead of the original drainage volume $V_p(t)$. The effective drainage volume should consider the change of reservoir properties because of the compaction effects. Due to the decrease of reservoir permeability and porosity (and hence changes in diffusivity, α) during pressure depletion, the effective drainage volume should be smaller than the original drainage volume.

To account for this, we run the fast marching again from the beginning to time t with the updated reservoir properties to get the effective drainage volume. Here, we can simply use a permeability multiplier, for example, a function of reservoir pressure as in Fig.9, to represent this compact effect.

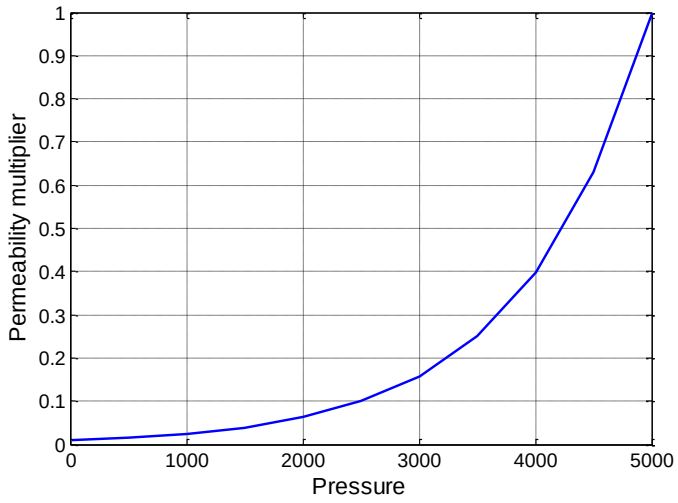

Fig.9 Permeability multiplier due to reservoir compaction as a function of reservoir pressure

The pressure drop is now calculated as

$$\Delta p = -\frac{q_{well}\Delta t}{c_t V_{p,eff}(t)} \qquad \text{Eq.27}$$

This pressure drop will be applied to all the cells behind the pressure front. Once the pressure field is updated, the reservoir properties are also updated using a specified compaction model. We then move on to the next time step and repeat the procedure.

Fig.10 illustrates the idea of the effective drainage volume to account for the compaction effects. Solid lines show the pressure front at successive time steps t_1, t_2, and t_3. With the compaction effects, the drainage volumes given by the pore volumes enclosed by the dashed lines in the figure are used instead. The dashed line is obtained by a FMM solution at each time step with updated reservoir properties.

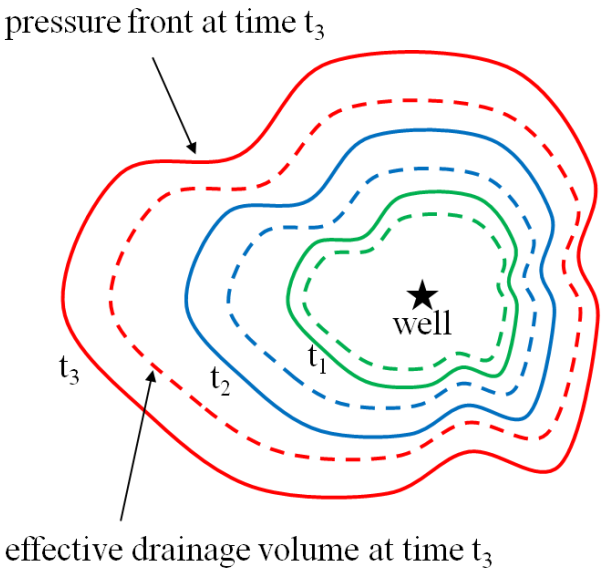

Fig.10 Illustration of the geometric approximation with and without the compaction effects

Fig.11 shows the influence on pressure response if we take the compaction effect into consideration. The synthetic reservoir model contains a horizontal well intersected by five hydraulic fractures, Fig.11a). The reservoir properties are listed in Table 1. We apply the geometric approximation to compute the well bottom-hole pressure under rate

constraints. As shown in Fig.11b), the effective drainage volume, which is smaller, results in a larger pressure drop so as to maintain the same flow rate.

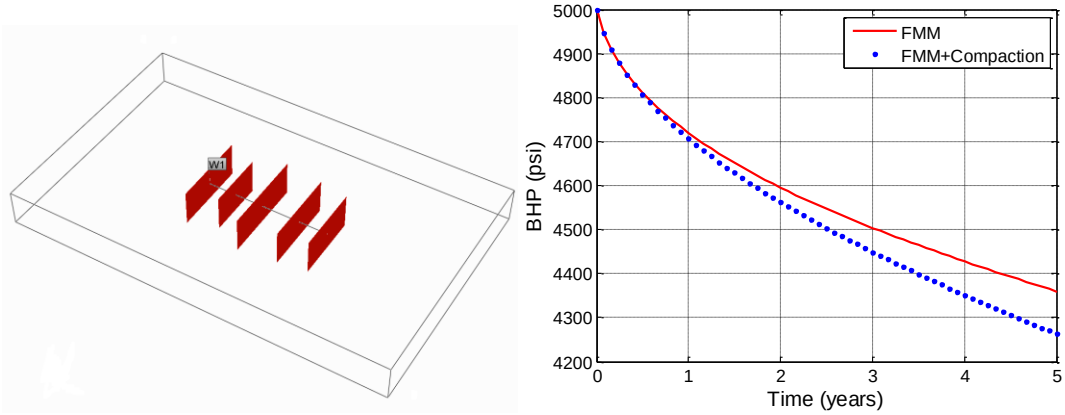

(a) (b)

Fig.11 a) Illustration of the reservoir model; b) Comparison of bottom-hole pressure calculated using the FMM approach with and without reservoir compaction effects.

Table 1. Properties for synthetic horizontal well with five stage fractures

Property	Value
Reservoir dimension (ft)	2505×4005×75
Fracture half length (ft)	400, 300, 450, 400, 350
Reservoir porosity	0.15
Gas viscosity (cp)	0.015
Initial reservoir pressure (psi)	5000
Matrix permeability (md)	0.0007
Fracture permeability (md)	10
Reservoir Temperature, T (˚F)	175
Total compressibility (psi-1)	2×10-4
Production Rate(Mscf/day)	200

2.6 Comparison with Finite Difference Simulator

To obtain confidence with our proposed approach, we compare the simulation results given by our method with finite difference simulator (CMG here) results (Fig.12-13). In Fig.12, it is the well bottom-hole pressure response for model shown in Fig.11. The model parameters are the same in Table 1. We also demonstrate a synthetic shale oil model, which has a hydraulic fracture associated with an enhanced permeability region in homogenous reservoir (Fig.13 a). Parameters for the synthetic reservoir model are listed in Table 2. The model is constant bottom-hole constrained, and production rate is calculated. The constant c=2 and 4 in Fig.13 b) are the transformation geometric factor between the diffusive time of flight and physical time for linear and radial flow separately. As in this case, both early linear flow and bilinear flow exist, we roughly take the geometric factor for linear and radial flow as boundary of the rate approximation. In both cases, the FMM and CMG have exactly the same reservoir properties and inputs. We can observe that the FMM simulation results agree with the results obtained by finite difference reservoir simulator.

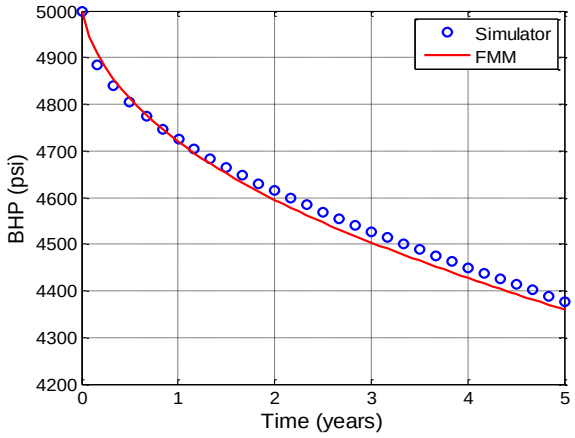

Fig.12 Well bottom-hole pressure calculated by the FMM approach compared with the reference solution obtained by finite difference reservoir simulator

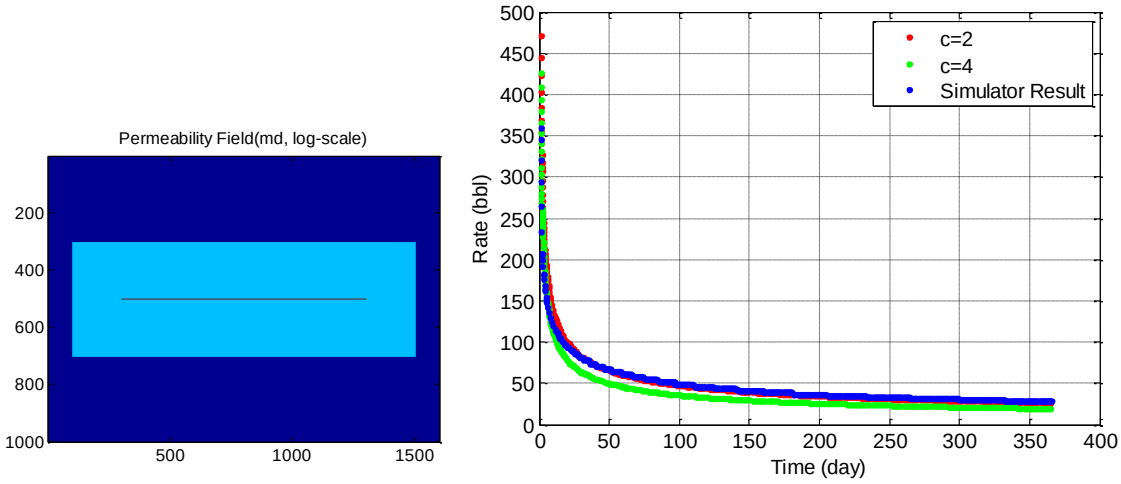

Fig.13 a) a hydraulic fracture with enhanced permeability region in homogeneous reservoir (permeability field); b) rate calculated by the FMM approach compared with CMG result

Table 2. Properties for synthetic one stage fracture with EPA

Property	Value
Reservoir dimension (ft)	800×500×1
Grid Size	2×2×75
Fracture half length (ft)	500
Reservoir porosity	0.2
Oil viscosity (cp)	0.35
Initial reservoir pressure (psi)	5000
Matrix permeability (md)	0.0005
Fracture permeability (md)	10
Total compressibility (psi-1)	3×10-5
BHP control (psi)	2000

3. MODEL CALIBRATION METHOD: GENETIC ALGORITHM

Matching the history data and calibrating the reservoir models are essential to predict future behavior with confidence and to perform computer experiments on methods of managing the reservoir (Oliver and Chen 2011). By calibrating the reservoir models, we mean adjusting the values of the model parameters such that the mathematical model of the reservoir can reproduce the observed behavior as close as possible. It generally involves an inverse problem, the history matching process.

3.1 Overview of Methods for History Matching

There is a number of ways to calibrate the model by matching history data. Initially, model calibration or history matching has commonly been conducted on a single deterministic model by a tedious and time consuming trial-and-error approach. In manual history matching, a structured approach is widely used where the sequence of scales of adjustments has been from global, then to flow units (regions), followed by local changes in model parameters (Cheng et al. 2008). The quality of manual history matching result heavily depends on the experience of the reservoir engineers. And for large fields, this process becomes close to impossible to investigate relationships between the model responses and variations of different reservoir parameters.

The past decade has seen remarkable progress in the ability to generate simulation models to match large amounts of production data by assisted history matching methods. It is similar to manual history matching, except computers and software tools are employed to adjust the reservoir parameters rather than direct intervention of reservoir engineers. Assisted history matching can be treated as a minimization problem, whose

objective generally includes a predefined data misfit function and penalty terms to match the observed response. There are several approaches to such minimization (Yang and Watson 1987; Bissell et al. 1992; Reynolds et al. 1996; Oliver et al 1997; Datta-Gupta et al. 2001; Cheng et al. 2008) and they can be broadly classified into three categories: gradient-based, sensitivity-based, and derivative-free (or direct search) methods, respectively.

The gradient-based methods, such as Gauss-Newton method, are intuitive as long as a mathematical minimization of the objective function is well defined. But they generally converge slowly (Bissell et al. 1992) and easy to lead to the nearest local minimum from the starting point instead of the global minimum (Williams et al. 2004; Landa et al. 2005). Sensitivity-based methods, such as LSQR, are attractive because of faster convergence compared to the gradient-based methods. However, an integral and computational expensive part of the sensitivity-based history matching is the computation of sensitivity coefficients, which are the partial derivatives of the production response with respect to the reservoir parameters of interest. The streamline-based generalized travel-time inversion (GTTI) technique has proven to be an effective method for calculating the parameter sensitivities (Datta-Gupta et al. 2001; Cheng et al. 2005). It can analytically compute the parameter sensitivities involving 1D integration along streamlines, which can be generated from either a streamline or a finite-difference simulator.

Most of the history matching approaches generally start with a single initial geological model and give a deterministic final model, which might not capture the reservoir

uncertainty appropriately if the initial model is far from representative. On the other hand, the solution to a history-matching process in reservoir simulation studies is not unique and multiple solutions are common. Derivative-free global search algorithms are preferred to local search as it can avoid the problem of converging to local optimum and also quantify the uncertainty of our matching result. The simulated annealing (SA) (Ouenes et al. 1994), Markov chian Monte Carlo (MCMC) (Sambridge and Mosegaard 2002; Ma et al. 2008), Ensemble Kalman Filter (EnKF) (Zafari and Reynolds 2005) and genetic algorithms (GA) (Holland 1992; Cheng et al. 2008) have proven to be effective for derivative-free history matching. The problem of derivative-free approach is that it requires numerous flow simulations, which could be computationally prohibitive for large field-scale models. Apart from the advances in parallel computing and faster computer processing speed, we can utilize surrogate models to improve the performance of derivative-free approaches.

3.2 Genetic Algorithm

Genetic algorithm is one extensively applied method for derivative-free assisted history matching (Schulze-Riegert et al. 2002; Williams et al. 2004; Cheng et al. 2008; Yin et al. 2011). The genetic algorithm imitates the biological principles of evolution---survival of the fittest. Solutions are represented as binary strings of 0's and 1's (Yin et al. 2011). The fitness of each individual is evaluated based on their performance, measured as a fitness function. The genomes or chromosomes, which are the full binary string containing all variables, start from a randomly generated population and multiple individuals are stochastically selected to be directly manipulated through crossover and

mutation, to generate a new generation. For genetic algorithm, crossover is the dominant operator while mutation is mainly used for keeping the genetic diversity of the population (Cheng et al. 2008). Commonly, the algorithm terminates when a satisfactory fitness level or the maximum number of generations has been reached.

3.2.1 Basic Concepts of Genetic Algorithm

In genetic algorithm, the parameters are generally expressed as binary strings of 0's and 1's, called genotype. When evaluating their fitness, the binary strings should be decoded into phenotype and then, the objective function can be calculated. Imitating the biological principles of evolution (the survival of the fittest), the parameter sets with smaller data misfit have larger fitness.

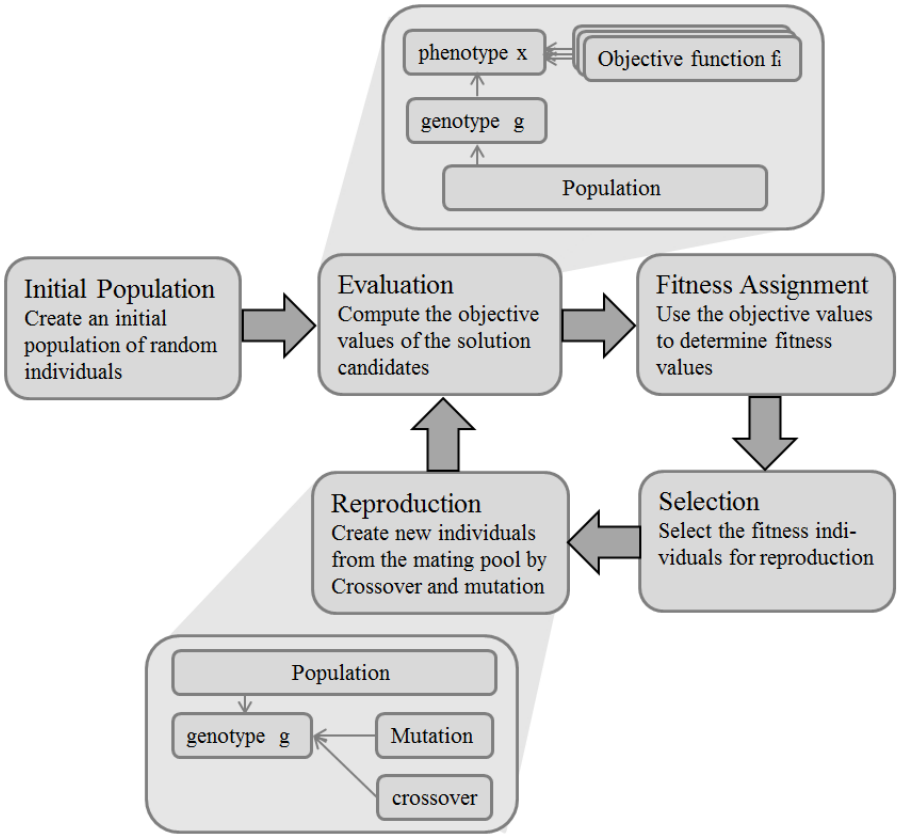

Fig.14 The basic cycle of genetic algorithms

To start with, a diverse set of models comprising the initial population is created either randomly or within an experimental design framework (e.g. Latin hypercube sampling or space filling strategy). The objective function of the current population is calculated, and then fitness values are assigned to each sample according to their objective values. The genetic algorithm selects a percentage of the population based on the value of fitness for breeding a new generation. The selection process is stochastic and random in nature. Genetic operators, mutation and/or crossover, are then utilized to reproduce a new generation. This process is repeated, as shown in Fig. 14 (Weise 2008).

3.2.2 Basic Operators: Crossover and Mutation

Crossover is the key process of creating new samples, or offspring, by recombining old samples. It is assumed that recombination of fitter parents will reproduce well and even better performing offspring, thus accomplishing the major objective of increasing the fitness function. This operator randomly chooses locations and exchanges the subsequences before and after those locations between two parameter vectors. There are typically three types of crossover operation, as shown in Fig.15: single-point crossover, multi-point crossover, and uniform crossover. For single-point crossover, one single position is randomly chosen and parents swap their binary bits with each other; in multi-point crossover, genome are partitioned into several segments and each of these segments (except for the first segment) take a crossover probability to swap with the same segment of the other genome; and for uniform crossover, each pair of bits form two parents will take a probability to swap. Generally speaking, the uniform crossover introduces diversity faster than multi-point or single-point crossover.

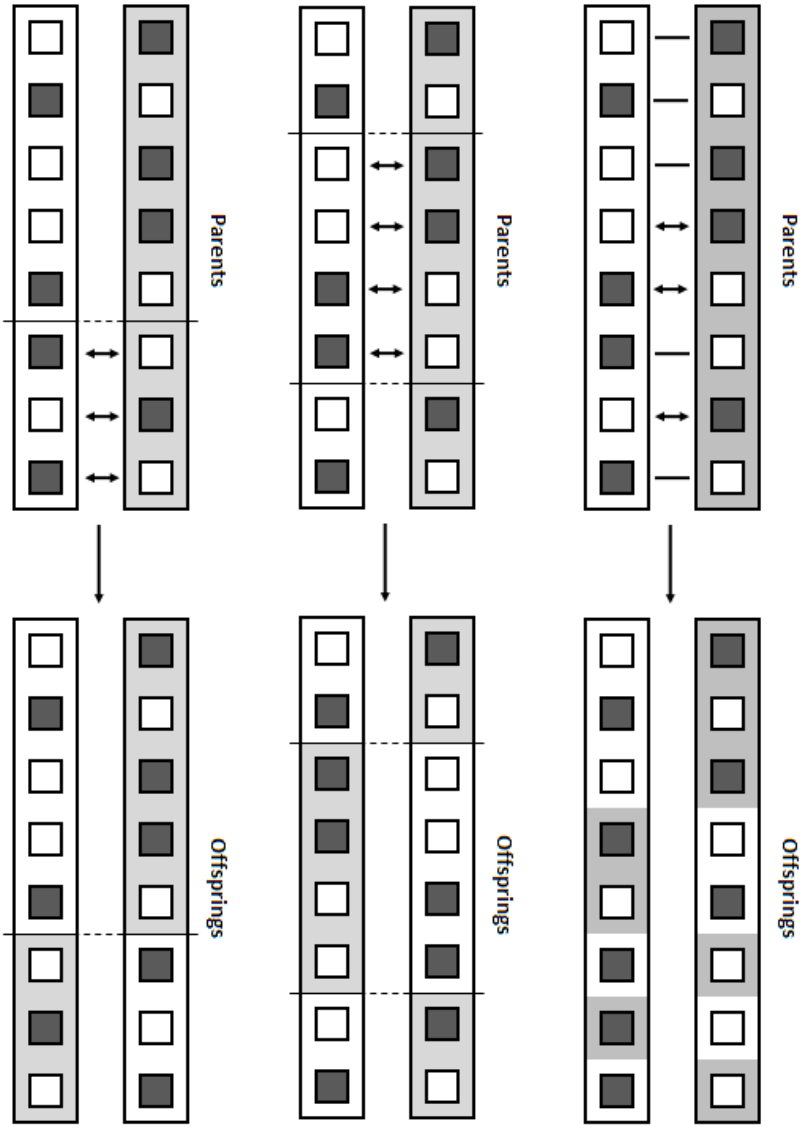

Fig.15 a) single-point crossover; b) multi-point crossover; c) uniform crossover

Mutation imitates “asexual” influences to a genome by, for example, environmental change. It is a key component to introduce new diversity to the generation though mutation is commonly paradoxical because most of them are harmful or at most neutral (Sawyer et al. 2007). This operator randomly flips some of the bits in binary form parameters (Fig.16). Mutation can occur at each bit position in a string with some

probability, which is usually very small. The mutation step typically follows crossover for each combined sample of string. For an optimization process, most of the hill climbing is via crossover while occasional mutation forces trial over all space, providing chances to find the global optima.

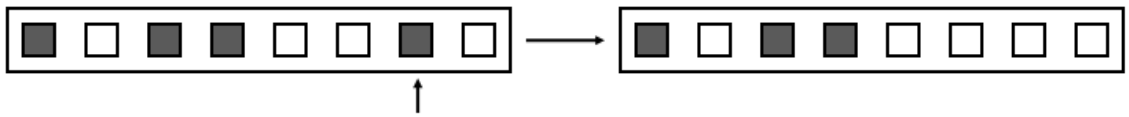

Fig.16 Uniform mutation

3.2.3 GA Based GLOBAL Software

GLOBAL software is a C++ based code, which can automatically adjust the input parameters for commercial reservoir simulators, like Eclipse, CMG, UTCHEM etc. It has used the genetic algorithm, one of the evolutionary algorithms, for calibrating global parameters. The flowchart is shown in Fig.17. In order to more effectively select the large amount of samples proposed by genetic algorithm, a proxy model is used.

To start with, experimental design is used to generate a response surface to guide the history-matching process (calculating sensitivity of each parameters is also an option in GLOBAL). Then GA generation are initialized or updated, and genetic operations are implemented. Instead of evaluating each sample by running simulation, the proxy checks it before going to the simulation step. The proxy check process estimates the objective function value from the response surface. Only the samples, whose estimated values satisfy the fitness criteria, will proceed to simulation; and that fails to pass the proxy check are discarded, making the genetic algorithm work more efficiently. After evaluating one whole generation, a converge criteria is checked. If it is satisfied, we can

exit and use final models for cluster analysis or locally update these models. If the convergence is not satisfied, then these evaluated samples are added into the proxy pool, thus proxy is updated, and then the GA process is repeated until convergence or satisfactory reservoir models are found.

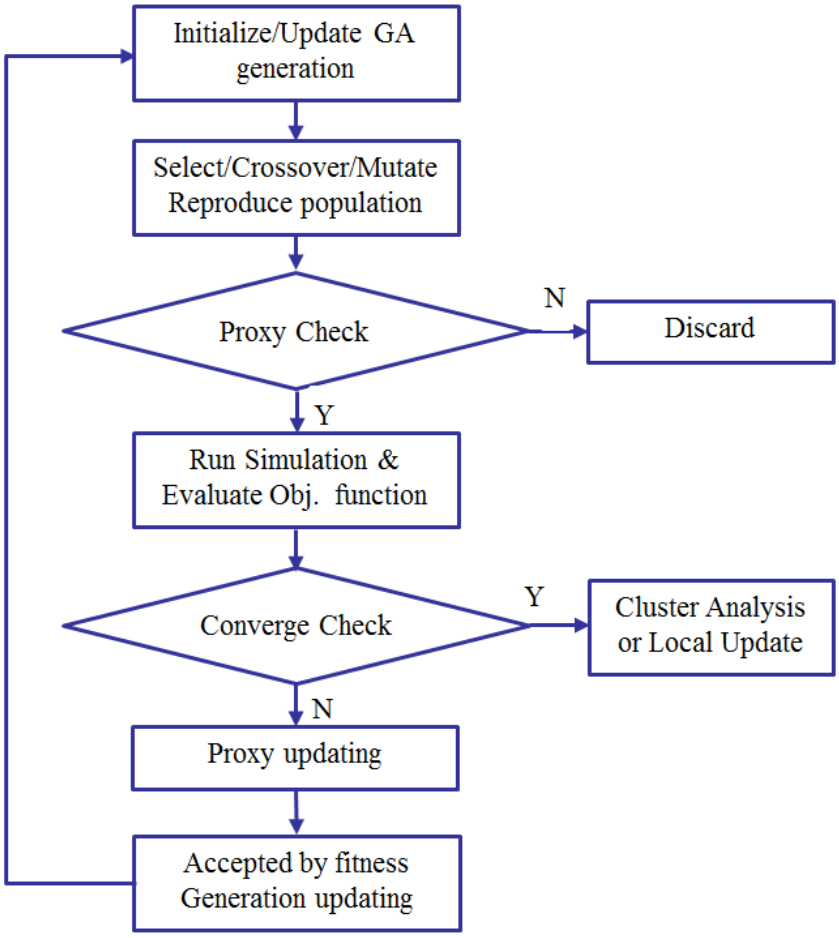

Fig.17 Flowchart of GA with proxy

4. INTEGRATED WORKFLOW: APPLICATION*

In this chapter, we apply our integrated workflow to a horizontal well with multistage hydraulic fractures in a shale gas reservoir. This example is designed after a real field case. The fast marching method is applied to approximate the reservoir response and the genetic algorithm approach is utilized here to modify reservoir parameters to match reference results. In addition, synthetic microseismic events are included to constrain parameter ranges for model calibration. The power and utility of this integrated workflow has been illustrated through this synthetic shale gas reservoir application.

4.1 Model Setup and Workflow

In our synthetic models, four hydraulic fractures are included (Fig. 18), constrained by four stages of synthetic seismic events (Fig. 19). The reservoir has about 0.3 million grids, and is constant bottom hole pressure (1000psi) constrained, as it is most of the cases in field practice in unconventional reservoir development. More details of the properties setting can be found in Table 3.

We have three kinds of permeabilities in this model: fracture permeability, matrix permeability and enhanced region permeability. We use a set of reference parameters to generate one year 'observed' gas production rate with fast marching method. The genetic algorithm varies the three types of permeabilities and the geometrical parameters associated with these four fractures to match the reference data. Then the uncertainty of

* Reprinted with permission from "Integration of Shale Gas Production Data and Microseismic for Fracture and Reservoir Properties Using Fast Marching Method" by Xie, J., Yang, C., Gupta, N., King, M. J., and Datta-Gupta, A., 2012. Paper SPE 161357 presented at SPE Eastern Regional Meeting, Lexington, Kentucky, 3-5 October. Copyright 2013 by SPE.

the reservoir parameter and performance are examined. After obtaining calibrated parameters, performance and stimulated reservoir volume (SRV) can also be estimated.

Table 3. Properties for synthetic horizontal well with multistage fractures

Property		Value	Unit
Reservoir	Size	2640×2280×50	ft^3
	Grid number	264×228×5	---
	Porosity	0.042	---
	Initial pressure	3000	psi
	Temperature	275	^oF
Fluid	Viscosity	0.03	cp
	Total compressibility	5.0E-4	psi^{-1}
	Gas expansion factor	1.404	Mscf/bbl
Well/Fracture	Bottom hole pressure	1000	psi
	Fracture number	4	---
	History matching time	365	day

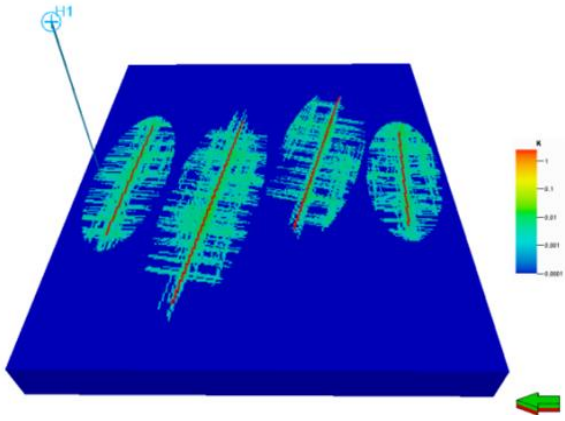

Fig.18 Sketch of model: horizontal well with 4 hydraulic fractures

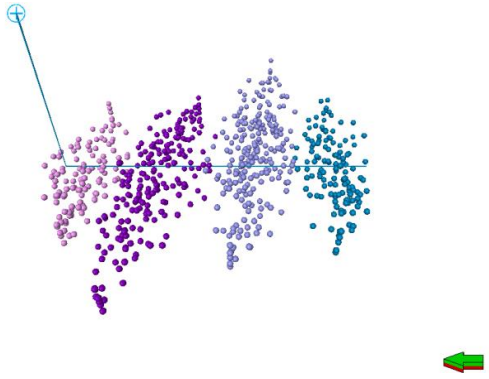

Fig.19 Four stages synthetic seismic-events

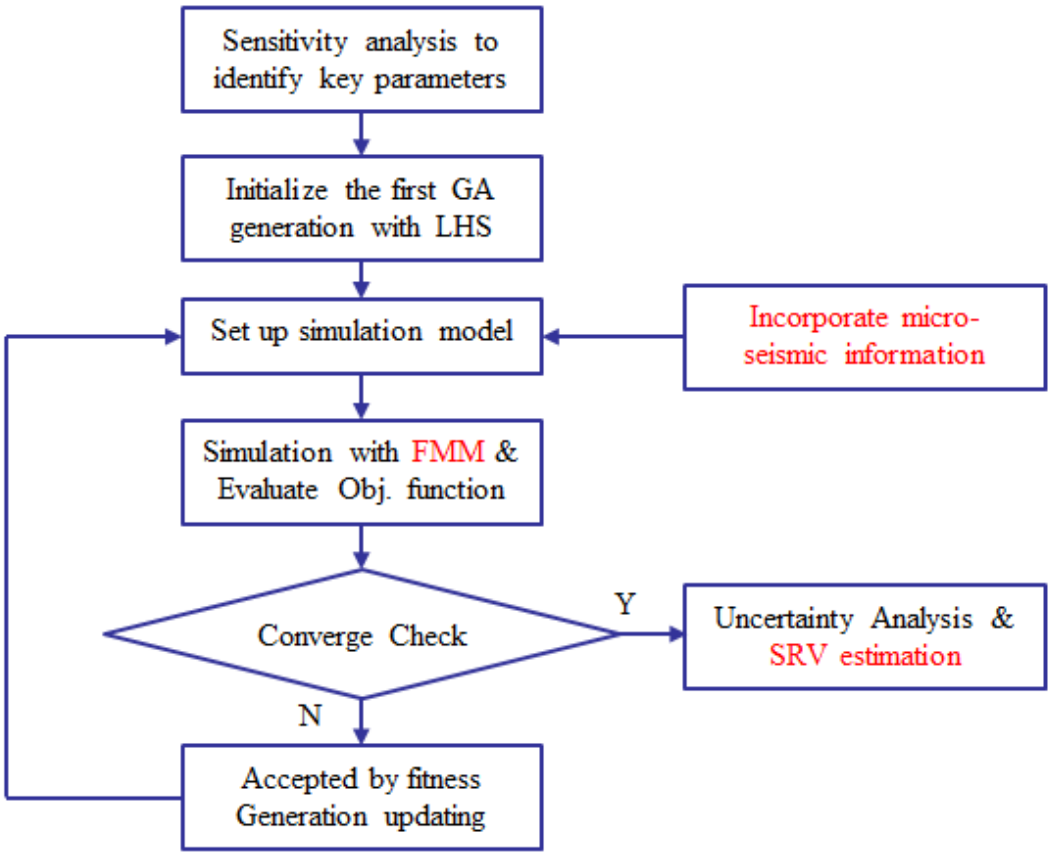

Fig.20 Integrated workflow for GA and FMM

Our workflow details of using a modified genetic algorithm to adjust shale gas reservoir and fracture parameters to calibrate the model can be found in Fig. 20. First, key parameters are identified using sensitivity analysis. Latin Hypercube Sampling (LHS), with a space filling design, is used to construct an initial generation. Unlike simple random sampling, the LHS can ensure a full coverage of the range of each variable by maximally stratifying each marginal distribution. Microseismic events are incorporated to construct a heterogeneous permeability field. Then, each member of the GA population is evaluated by running the simulation, based on fast marching method and geometric approximation method. This process is repeated and generations are updated

until the convergence criteria are satisfied or after obtaining satisfactory results. With the matched models, we can check the uncertainty of parameters or reservoir response, and the estimated SRV.

4.2 Integration of Micro-seismic Events

Microseismic mapping measurements have recently been utilized to help interpreted large scale complex hydraulic fracture propagation, especially in unconventional reservoirs (Maxwell et al. 2002; Cipolla et al. 2011, 2012). The nature of fracture complexity must be clearly understood to select the best stimulation strategy and completion design. Cipolla et al (2011) recently proposed two main complex hydraulic fracture models to better understand hydraulic fracture complexity, namely unconventional fracture model (UFM) (Fig.21) and wire-mesh model (Fig.22).

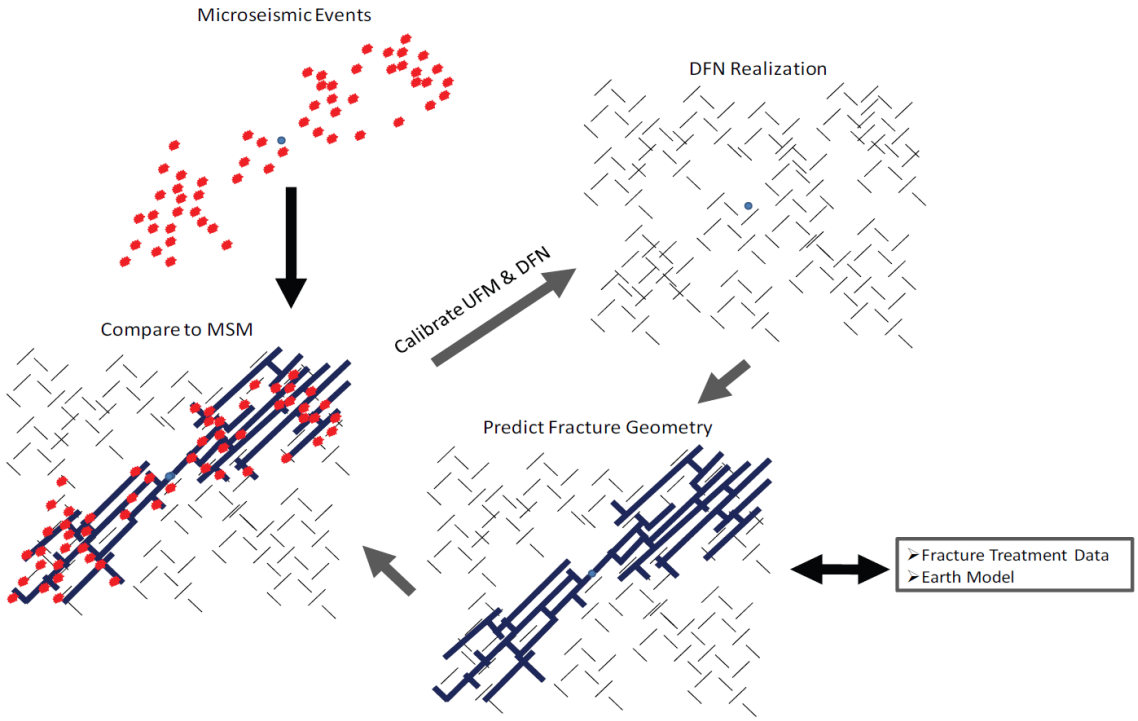

Fig.21 Unconventional facture model (UFM) workflow

It is required for UFM workflow to generate natural facture network or discrete fracture network (DFN) based on geological, geophysical, and/or log-based data. Fracture treatment data and earth model are input and fracture geometry is generated using a DFN. Then, the generated fracture geometry is then compared to the microseismic event pattern for consistency. The UFM net pressure should be consistent with the treatment data. The uncertainty in microseismic events locations and the possibility that some events are induced by stress or poroclastic effects should also be taking into account. If the model net pressure is not consistent with actual measurements, or UFM fracture geometry is not consistent with microseismic event patterns, the UFM input parameters are attuned and another DFN realization is selected. The modification of UFM input parameters will be dictated by the availability and reliability of data, typically maximum horizontal stress and mechanical properties of the nature fractures.

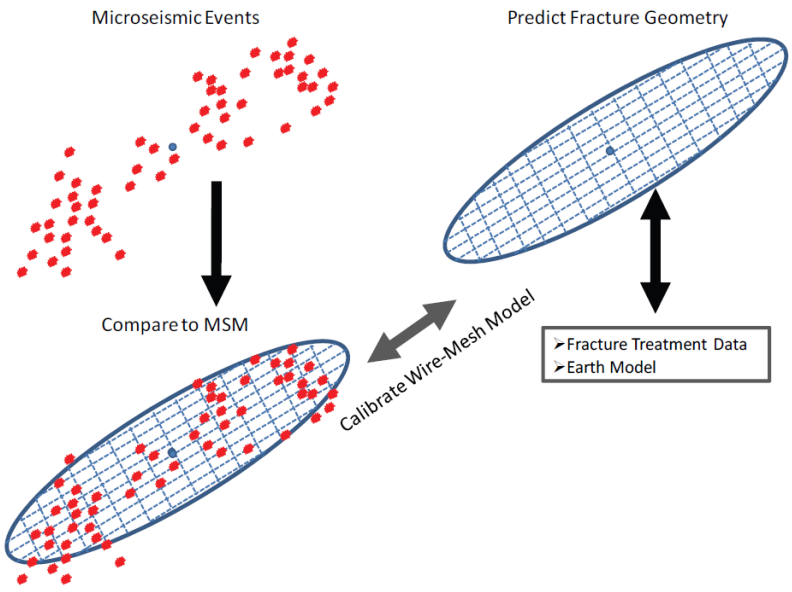

Fig.22 Wire-mesh model workflow

The major difference between the Wire-mesh and UFM is that the Wire-mesh model does not require DFN. The Wire-mesh model is pretty straight forward. The fracture treatment data and Earth model information are input into the Wire-mesh model. Three major parameters, maximum horizontal stress, fracture spacing and roughness factor, are calibrated to make the predicted complex fracture geometry consistent with the physics. The basic shape of microseismic events can be matched by adjusting the maximum horizontal stress and actual net pressure can be matched through modifying fracture spacing and roughness factor.

Inspired by and analogous to the UFM and wire-mesh model described by Cipolla et al (2011, 2012), we proposed our method of modeling complex fracture network (Fig.23). Instead of comparing the complex fracture geometry induced by fracture treatment data and Earth model with microseismic pattern and net pressure, we simply start with the microseismic events describing the density of natural fractures. We have a primary fracture and an associated ellipsoid stimulated region in each fracture stage. First, the primary fracture in each stage is defined, following the orientation of the microseismic cloud of that stage. Considering the uncertainty of microseismic event locations and the chance that some events are induced by stress or poroclastic effects, the fracture half-length x_f and the size of the stimulated region are not fixed and can be calibrated to match the reservoir performance. We define the ellipsoid of the stimulated region with three axes a, b and c. The effect of stimulated region does not heavily depend on the specific shape of the region, but the actual stimulated reservoir volume matters more. In order to reduce the number of calibration parameters, some additional constraints are

applied. The axis in z direction, c, is fixed at twice the reservoir thickness to represent a fully penetrated fracture. The minor axis, b in horizontal plane can vary within a specified range, while the major axis a is constrained from fracture half length (we assume $a = x_f + b$). By using this relationship, we can ensure that the SRV extends beyond the fracture half-length.

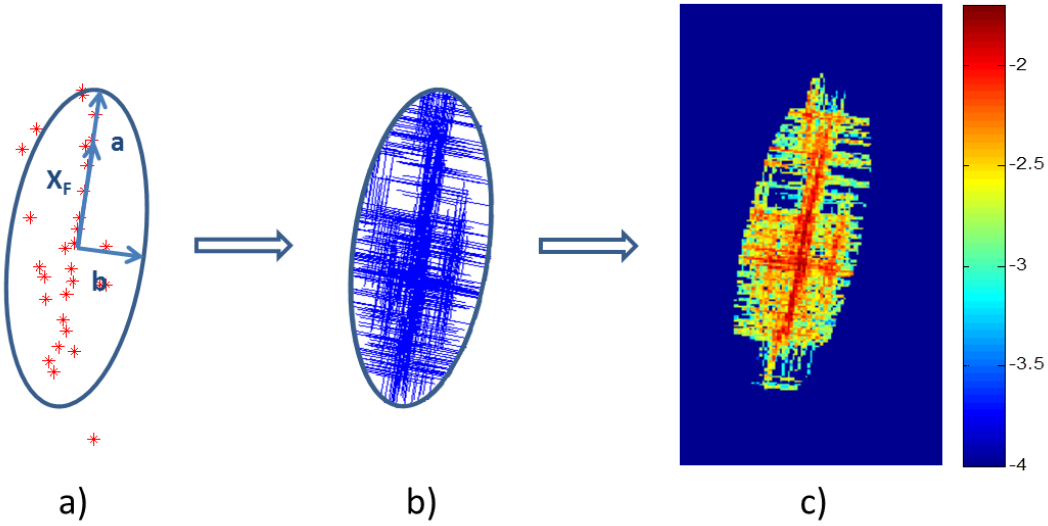

Fig.23 Proposed workflow to integrate microseismic information, a) microseismic events; b) a DFN model; c) generated heterogeneous permeability field

The microseismic events beyond the ellipsoid are discarded to account for unreliable microseismic events far away from perforation. The DFN model is used to generate natural fracture network around each microseismic event within the ellipsoid. The natural fractures follow certain geostatistical properties (mean and standard deviation for fracture length and height) but are assumed to be orthogonal and with fixed azimuths. The fracture properties (permeability, height and length) are then assigned to each

simulation grid to calculate a property, $I = \sum khl$. The effective permeability in the stimulated region is then linearly distributed from the property: maximum value corresponds to enhanced permeability k_E, and minimum value corresponds to matrix permeability k_M. The result is a heterogeneous permeability field constrained to microseismic events inside the ellipsoid. Notice that all the four facture stages share the same value of enhanced permeability k_E and fracture permeability k_F.

Fig. 24 shows an example of a generated permeability field according to the approach we described above. If we filter out the matrix part, Fig. 25 gives us an idea of stimulated regions. It is worth mentioning that our SRV is actually less that the volume of the ellipsoid because part of grid within the ellipsoid, which has the same value with matrix permeability, is treated as matrix. Further, along with other properties, the generated permeability field can be input into our forward model, fast marching method and geometric approximation, to obtain simulation results (Fig.26): arrival time map (a), drainage volume versus time (b), and production rate versus time (c).

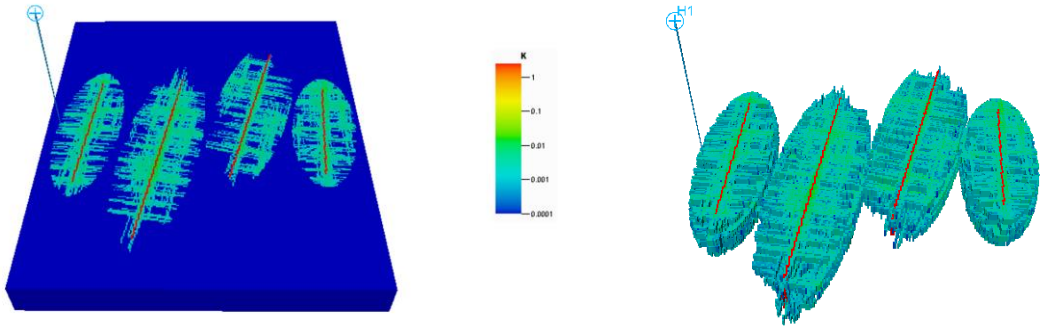

Fig.24 Genearted permeability field

Fig.25 Visualization of the stimulated region

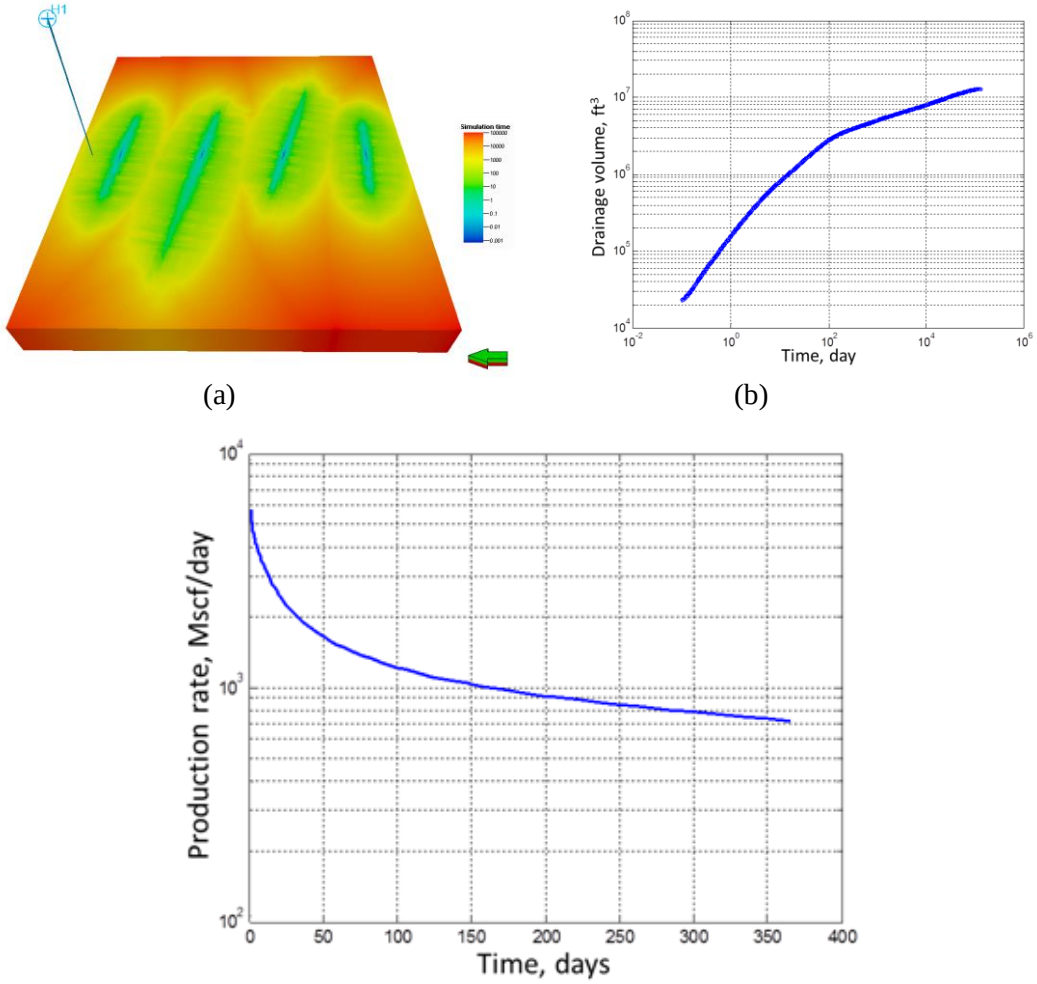

(a) (b)

(c)

Fig.26 Simulation results for FMM and geometric approximation: a) Arrival time (days); b) Drainage volume vs time(log-log scale); c) Production rate vs time(semi-log scale)

4.3 Parameter Estimation and Calibration Results

The parameters to be estimated via history matching and the associated uncertainties are listed in Table 4. They are the permeabilities for the matrix, the enhanced region, the fracture, and also, the fracture half-length and the minor axes associate with these fractures. A uniform distribution assumption is applied to these parameters. The observation data is generated from the reference parameter set, which is also shown in

Table 4. The horizontal well is modeled at a constant bottom-hole pressure (BHP) of 1000 psi. The first year gas production data is utilized to calibrate the model parameters and an additional four year well performance prediction is made. As discussed above, the fast marching method and the geometric approximation method are applied to simulate the rate response. The objective function, i.e. the misfit, for history matching is defined as the sum of the squared differences of production rate between the simulation results and the reference.

Table 4. History matching parameters ranges and the reference values

Uncertainty Variables	Base	Low	High	Reference
Matrix permeability (k_M)	12E-5 md	8E-5 md	15E-5 md	10E-5 md
Enhanced permeability (k_E)	0.022 md	0.005 md	0.05 md	0.02 md
Fracture permeability (k_F)	2.4 md	0.5 md	4.0 md	2.50 md
Fracture1 half length (X_{F1})	390 ft	300 ft	530 ft	400 ft
Fracture2 half length (X_{F2})	600 ft	400 ft	800 ft	650 ft
Fracture3 half length (X_{F3})	600 ft	350 ft	700 ft	550 ft
Fracture4 half length (X_{F4})	320 ft	250 ft	450 ft	300 ft
Ellipsoid1 minor axis (b_1)	180 ft	150 ft	250 ft	200 ft
Ellipsoid2 minor axis (b_2)	260 ft	200 ft	300 ft	250 ft
Ellipsoid3 minor axis (b_3)	230 ft	200 ft	300 ft	250 ft
Ellipsoid4 minor axis (b_4)	190 ft	170 ft	230 ft	200 ft

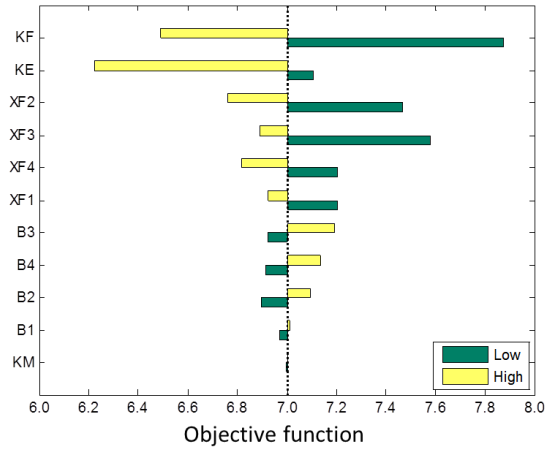

Fig.27 Sensitivity analysis of history matching parameters

A sensitivity analysis is performed with one-year simulation to evaluate the relative influence of various parameters. The sensitivity results are showed in a tornado plot (Fig.27). The line in the middle, approximately has a value of 7, shows the objective function of the base model. We vary one parameter at a time, keeping others at the base values, and rerun the simulation. High (yellow) and low (dark green) correspond to the impact of high and low bounds of each parameter. From the sensitivity results, we can easily identify that the fracture permeability and enhanced region permeability have the most significant influences, followed by the half-lengths of the four fractures. The matrix permeability has the least influence. This is due to the short simulation time period during which the pressure disturbance has not reached the matrix yet.

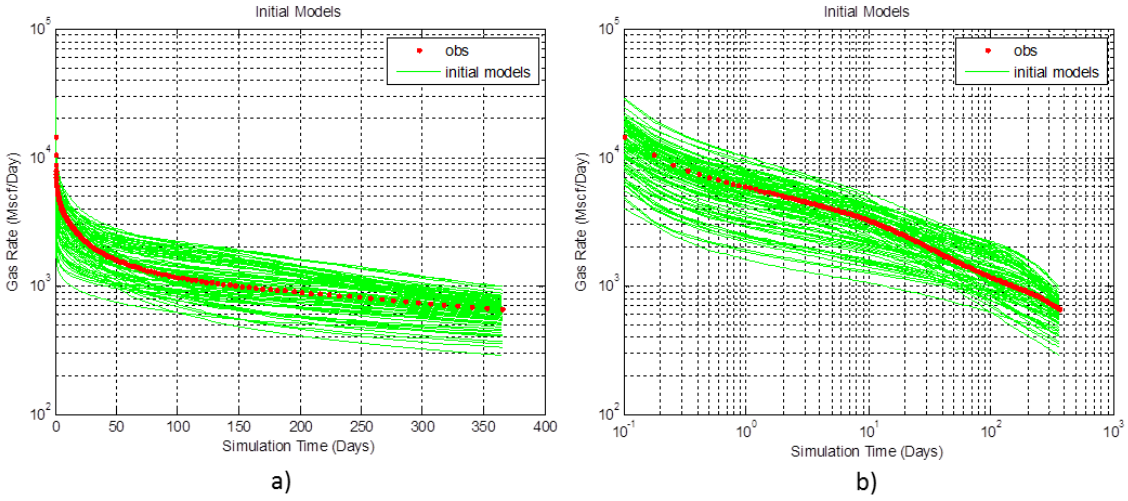

Fig.28 Simulation results with initial eighty models (green) compared to reference model (red): a) in semi-log scale; b) in log-log scale

The genetic algorithm is carried out for 15 generations and each generation has 80 realizations. The gas production rate for the first generation is shown in Fig. 28, both semi-log and log-log plots. The red dots indicate the results for the reference model, and

the green lines correspond to the initial models. It is easy to notice the wide range of predictions from the initial models, indicating large parameter uncertainties. After 15 generations, the misfits for all members versus generation number are plotted in Fig.29. Clearly, a decreasing trend of the objective function can be observed (considering that the value of misfit is in logarithmic form).

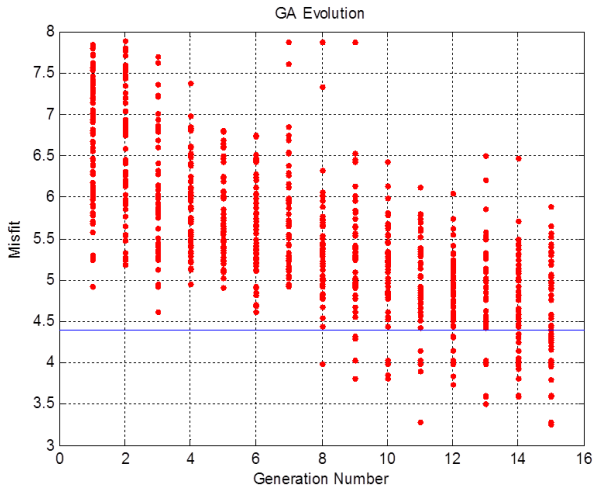

Fig.29 The objective function versus generation number

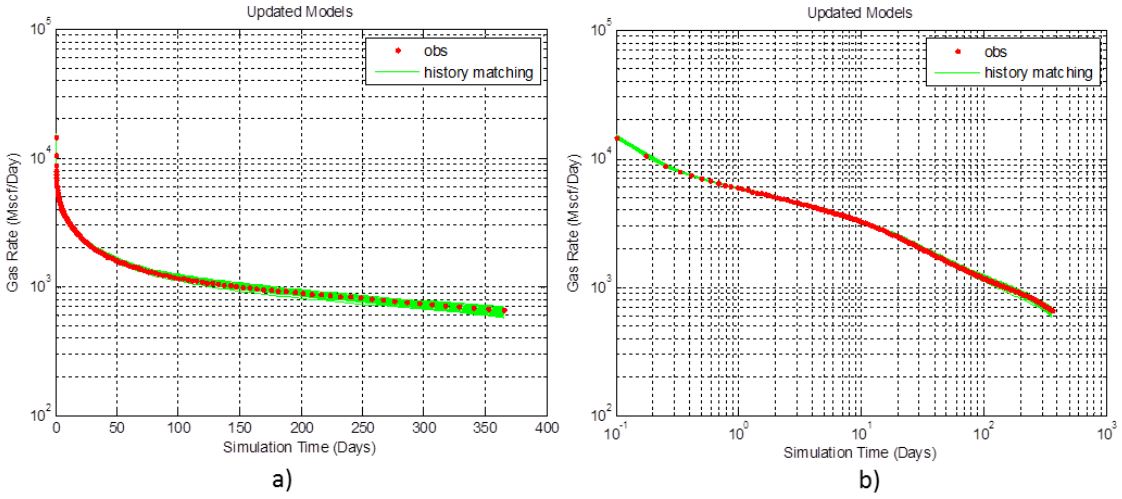

Fig.30 Selected fifty models (green) compared to reference model (red), a) in semi-log scale; b) in log-log scale

We select the best 50 models with a misfit cut-off as shon by the horizontal line and plot the well gas production rate for these models in Fig. 30. The reference data is matched quite well and uncertainties reduce significantly compared to the initial models. The effectiveness in model calibraiton can also be explaind by comparing the initial and the updatd fracture permeability, enhanced region and matrix permeability after history matching. These resutls are summarized in boxplot of permeability in Fig. 31. These permeabilities are normalized to be range between zero and unity here. The range of model parameters in the final population is indicated by the blue box with reference indicated by the triangle. The red line stands for the median. After hitory matching of the first year production data, the uncertainty range of the fracture and enhanced permeability converge to the reference with very narrow uncertainty ranges. That's because they are very sensitive to the produciton response (shown from the sensitivity analysis). The uncertainty range of the matrix permeability didn't reduce so much; it is because this parameter can not be well calibrated within just one year simulation.

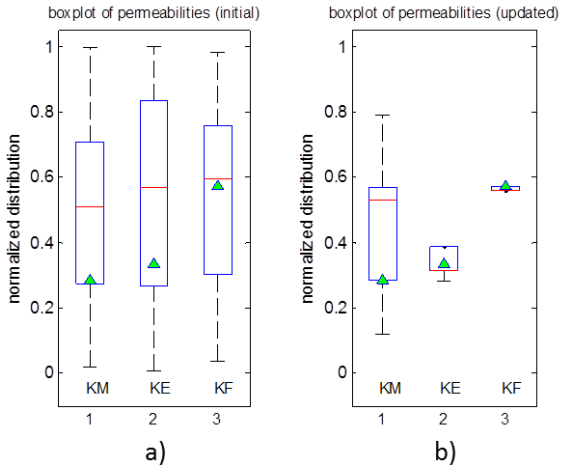

Fig.31 Permeability (fracture, enhanced and matrix) uncertainties: a) initial range; b) updated range

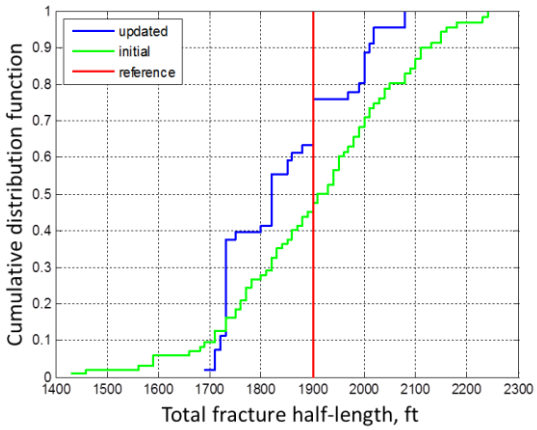

Fig.32 CDF plot of total fracture half-length

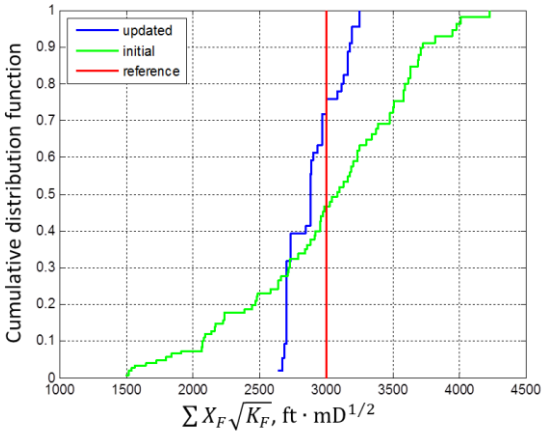

Fig.33 CDF plot of $\sum x_f \sqrt{k_F}$

We also estimate the fracture half lengths in each stage during the calibration. Instead of examining the individual stage fracture half lengths which are likely to vary considerably, we compare the total fracture half lengths from all stages and plot the cumulative distribution functions (CDFs) for the initial models (green) and the updated models (blue) as shown in Fig.32. The total fracture half length of the reference model is 1,900 *ft* as shown by the red vertical line. From these results, we can clearly see the reduced uncertainty in updated models as indicated by the reduced range and spread of the updated distribution compared to the initial distribution of total fracture half lengths. The mean and standard deviation of total fracture half-length for the updated 50 models are 1836 *ft* , and 116 *ft* respectively. This result compares very favorably to the reference model. In Fig.33, We have also shown the cumulative distribution of the composite quantity, $\sum x_f \sqrt{k_F}$, which is closely related to the flow across the fracture surfaces. The

results are shown in the same format in Fig. 32, and the reduction in uncertainty is even more significant here.

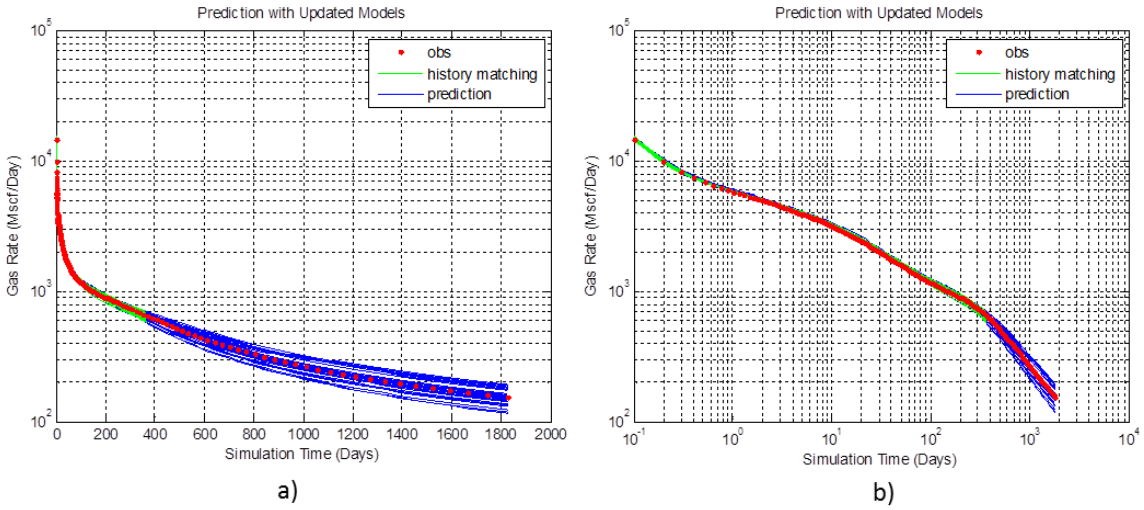

Fig.34 Four year predictions with updated models, a) in semi-log scale; b) in log-log scale

To further assess quality of model calibration and the associated uncertainties, additional four-year simulation is carried out to predict the well production performance (Fig.34). Green lines stand for history matching period and blue curves indicate prediction period. All of prediction lines give a gas rate interval of 0.1 – 0.2 $Mscf/d$ at the end of the fifth year. These suggest a very small range of gas production rate due to the model calibration. However, there are unresolved uncertainties. For example, the matrix permeability, which is not well constrained during the synthetic history matching process because the flow in first year is mainly inside the stimulated region. As the pressure front reaches the boundary of the stimulated region, matrix permeability plays a more and more important role in predicting the production rate. In future application, if

matrix permeability is as well calibrated as fracture and enhanced region permeability, we can obtain performance prediction with much more confidence.

4.4 Stimulated Reservoir Volume Estimation

From our drainage volume calculations, we can estimate the stimulated reservoir volume (SRV). As shown in Fig.7 (c), the first plateau in the drainage volume plot indicates the pore volume corresponding to the SRV. For this application, we plot drainage volume versus time in log-log scale for the reference and the fifty updated models in Fig.35. Because of the permeability heterogeneity in the stimulated region, we can only see the curves bending here instead of forming a distinct plateau. The inflection point in Fig.35, where we see a reversal in concavity is an indication of the SRV pore volume. The two dark green lines give us an estimate of the range of the SRV pore volume.

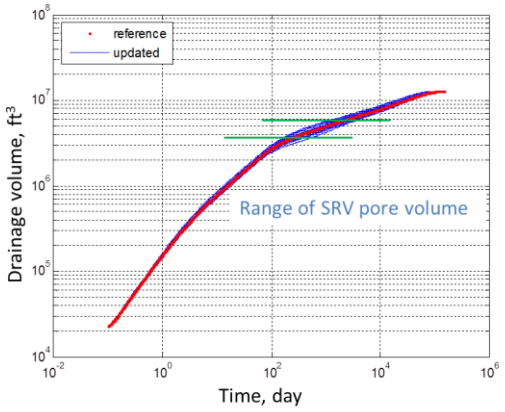

Fig.35 Drainage voule vs time (log-log scale)

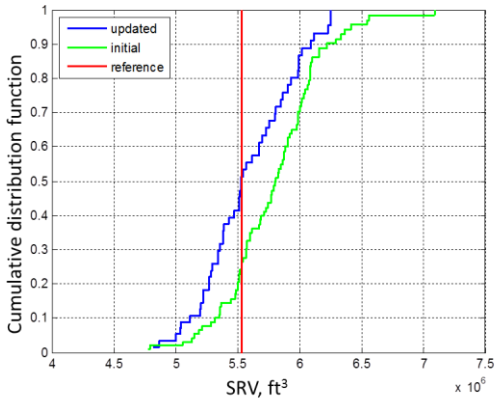

Fig.36 CDF plot of SRV pore volume

The CDFs of the SRV pore volume for the initial and updated models along with that of the reference model are plotted in Fig. 36. The SRV pore volume of the reference model is 5.534 *MMcf* . After history matching, the range of the updated SRV pore volume is

considerably reduced compared to that of the initial model as shown in Fig.36. The mean and standard deviation of the SRV pore volume from the updated models are 5.559 and 0.367 *MMcf* respectively.

As the total SRV matters more than the specific combination of half-lengths of the four fracture stages, we are less likely to come up with a very specific shape of these fractures, as long as the total stimulated reservoir volume is well calibrated. In Fig.37, The SRV shape of reference model is compared to the stimulated reservoir volumes of a selected set of the updated models. We can see that the SRV of each fracture stage can vary a lot while the total SRV pore volume is reasonably constrained. The reduced uncertainty in the estimated fracture parameters and the SRV leads to improved production forecasting and reserve estimation.

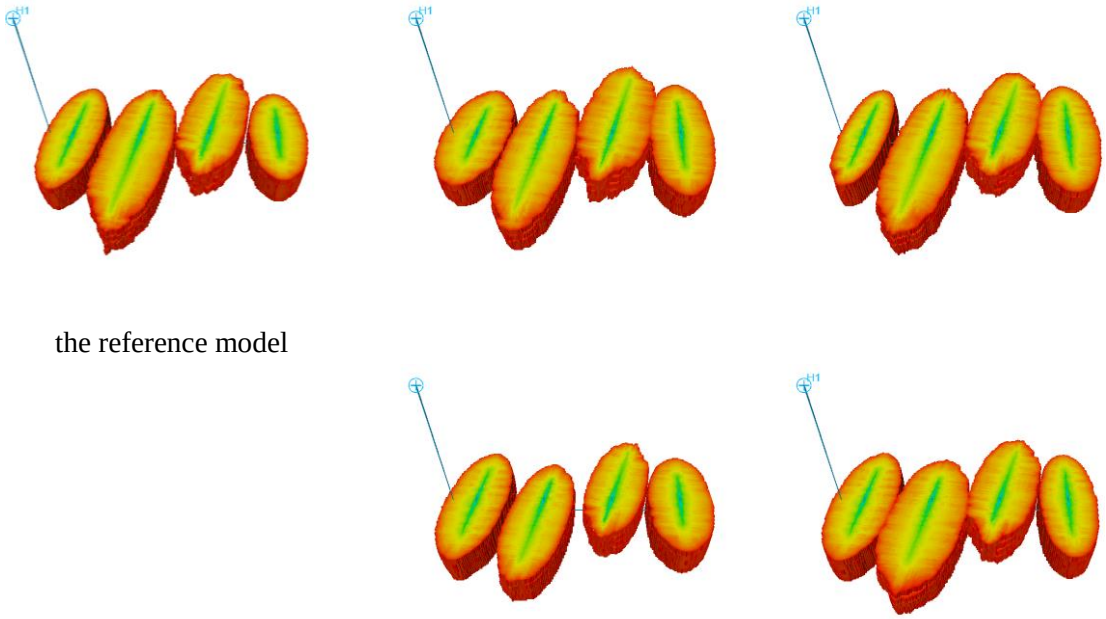

the reference model

Fig.37 SRV comparison, the reference versus four updated models

5. CONCLUSIONS AND RECOMMENDATIONS

5.1 Conclusions

This thesis demonstrates a novel approach to calculate drainage volume and well performance in shale gas reservoirs using fast marching method (FMM) combined with a geometric pressure approximation. This methodology can account for complex fracture geometry and reservoir heterogeneity. The genetic algorithm, a derivative-free direct search approach, is applied in our reservoir model calibration workflow. The power and utility of our approach has been illustrated using history matching of a shale gas well performance data. We have integrated microseismic events into a history matching workflow to calibrate fracture/matrix parameters for improved production forecast and estimate the SRV regions using calibrated models.

The main findings from this integrated workflow can be summarized below:

- The pressure front propagation in reservoirs follows an Eikonal equation obtained from an asymptotic solution of the diffusive equation. This Eikonal equation can account for reservoir heterogeneity, and be solved efficiently by applying a fast marching method (FMM). The fast speed of FMM makes it ideally suited for parameter calibration via inverse modeling.
- This algorithm provides a diffusive time of flight distribution away from the source, showing the ‘depth of investigation’ of the pressure front at all flow times. It extends the idea of radius of investigation, which is generally limited to homogeneous reservoirs with simple flow geometry.

- By adding up all the cell pore volumes behind the pressure propagation front, we can estimate the drainage volume of a well. It can also be easily visualized, describing how drainage volume increases with time after converting the diffusive time of flight into physical time with a proposed relationship.
- Based on the drainage volume provided by the FMM, a geometric approximation approach can be applied to estimate the reservoir performance, both well production rate under constant pressure constraint and well pressure behavior with constant rate constraint.
- Using FMM combined with geometric approximation, the stimulated reservoir volume (SRV) and estimated ultimate recovery (EUR) can be approximated. This is helpful for fracture design and other optimization problem.
- Some specific physics associated with shale gas reservoir, like reservoir compaction effects, can be taken into consideration.
- A stochastic global search approach based upon the genetic algorithm can decrease the possibility to converge to a local minimum. It works more effectively to match the global parameters when combining with a proxy model for the fitness function.
- Microseismic events have been utilized to help interpret large scale complex hydraulic fracture propagation. Here, microseismic information is utilized to constrain our factures. We also proposed a method to interpret microseismic information into heterogeneous permeability field.

5.2 Recommendations

All the proposed approaches, fast marching method, geometric approximation, integration of microseismic information, and model calibration via genetic algorithm, can help us better understand and investigate the performance of shale gas reservoirs. The results obtained are very encouraging. However, there is still scope for further investigation and improvements:

- Extend the application to more complex grid systems, such as variable grid size, local grid refinement and corner point grids, especially accurate calculation for the grids with large aspect ratio.
- Additional studies at high reservoir property contrast situation, for example, early time of pressure propagating from fracture to matrix.
- More physics of shale gas reservoir should be investigated and taken into consideration apart from reservoir compaction, like adsorption and desorption, Klinkenberg slippage, and Knudsen diffusion.
- More comprehensive and robust comparison with finite difference method based commercial simulator is still needed to increase our confidence.
- As for the genetic algorithm, it is also necessary to investigate how to reduce the possibility for generation collapse.
- Sensitivity based approach (the sensitivity of drainage volume or diffusive time of flight with respect to reservoir properties) might be developed to be applied to history matching.

NOMENCLATURE

A	area along the pressure front, ft^2 [m^2]
C_k	pressure amplitude at the k-th order in Fourier domain
D	standard difference operator
h	reservoir thickness, ft
i and j	grid index
k	permeability, md
k_F	fracture permeability, md
k_E	permeability in enhance region, md
k_M	matrix permeability, md
M	mass of gas, lbm [kg]
$m(p)$	pseudo-pressure, psi [kPa]
$\tilde{m}(p)$	pseudo-pressure in Fourier transformed domain, psi [kPa]
p	pressure, psi [kPa]
$\bar{p}$	reservoir average pressure, psi [kPa]
$\tilde{p}$	pressure in Fourier transformed domain, psi [kPa]
p_i	initial reservoir pressure, psi [kPa]
p_{wf}	well bottom hole pressure, psi [kPa]
Δp	pressure drop, psi [kPa]
p_{sc}	standard condition pressure, psi [kPa]
q	total gas rate SCF/D [m^3/d]

q_{res}	gas rate at reservoir condition SCF/D [m^3/d]
q_{well}	well gas rate SCF/D [m^3/d]
q_D	dimensionless gas rate
r	radius of investigation, ft
R	universal gas constant, ft^3 psi/[R lb-mol]
T	reservoir temperature, ^oF
T_{sc}	standard condition temperature, ^oF
t	time, hr [day]
t_p	pseudo-time, hr [day]
V_p	pore volume, ft^3
$V_{p,eff}$	effective pore volume, ft^3
$\vec{v}$	Darcy velocity, ft^3/second
$\vec{x}$	spatial coordinate vector, ft [m]
x	*x*-coordinate direction
x_f	fracture half-length, ft
y	*y*-coordinate direction
Z	compression factor, fraction
α	hydraulic diffusivity, md/ [cp • psi^{-1}]
β	geometric factor
π	mathematical constant, 3.141592…

c_t	total compressibility, psi^{-1}
μ	viscosity, cp [Pa • s]
ρ	gas density, lbm/cu ft [kg/m^3]
ϕ	porosity, fraction
τ	diffusive time of flight, $\sqrt{hr}$
ω	time in Fourier transformed domain

REFERENCES

Bissell, R.C., Killough, J.E., and Sharma, Y. 1992. Reservoir History-matching Using Method of Gradients on a Workstation. Paper SPE 24265 presented at the SPE European Petroleum Computer Conference, Stavanger, Norway, 25-27 May.

Cheng, H., Datta-Gupta, A., He, Z. 2005. A comparison of travel-time and amplitude matching for field-scale production-data integration: sensitivity, nonlinearity, and practical implication. SPEJ. **10**(1), 75-90. SPE 84570-PA.

Cheng, H., Dehghani, K., and Billiter, T. 2008. A Structured Approach for Probabilistic-Assisted History Matching Using Evolutionary Algorithms: Tengiz Field Applications. SPE 116212-MS.

Cipolla, C. L., Lolon, E. P., Erdle, J. C., and Tathed, V. 2009. Modeling Well Performance in Shale-Gas Reservoirs. SPE 125532-MS.

Cipolla, C. L., Weng, X., Mack, M.G., Ganguly, U., Gu, H. et al. 2011. Integrating Microseismic Mapping and Complex Fracture Modeling to Characterize Hydraulic Fracture Complexity. SPE 140185-MS.

Cipolla, C. L., Maxwell, S., and Mack, M. G. 2012. Engineering Guide to the Application of Microseismic Interpretations. SPE 152165-MS.

Clarkson, C. R., Nobakht, M., Kaviani, D., and Ertekin, T. 2012. Production Analysis of Tight-Gas and Shale-Gas Reservoirs Using the Dynamic-Slippage Concept. *SPE Journal* **17** (1): 230-242. SPE 144317-PA.

Datta-Gupta, A. and King, M. J. 2007. Streamline Simulation: Theory and Practice. SPE Textbook Series Vol.11.

Datta-Gupta, A. Kulkarni, K.N., Yoon, S., Vasco.D.W. 2001. Streamlines, Ray Tracing and Production Tomography: Generalization to Compressible Flow. *Petroleum Geoscience* **5**:75-86

Datta-Gupta, A., Xie, J., Gupta, N., King, M. J. and Lee W. J. 2011, Radius of Investigation and its Generalization to Unconventional Reservoirs, *Journal of Petroleum Technology*, **63** (7): 52-55.

Dong, Z., Holditch, S.A., McVay, D.A.2013. Resource Evaluation for Shale Gas Reservoirs. *SPE Journal* **5**(1):5-16. SPE 152066-PA.

Energy Information Administration (U.S. EIA). Annual Energy Outlook 2012, EIA-0383(2012): 93. http://www.eia.gov/forecasts/aeo/pdf/0383(2012).pdf

Fan, L., Thompson, J. W., and Robinson, J. R 2010. Understanding Gas Production Mechanism and Effectiveness of Well Stimulation in the Haynesville Shale through Reservoir Simulation. SPE 136696-MS.

Fetkovich M. J. 1980. Decline Curve Analysis Using Type Curves. *Journal of Petroleum Technology* **32** (6): 1065-1077.

Freeman, C. M., Moridis, G., Ilk, D. and Blasingame, T. A. 2009, A Numerical Study of Performance for Tight Gas and Shale Gas Reservoir Systems, SPE 124961-MS.

Holditch, S. A. 2010. Shale Gas Holds Global Opportunities. *The American Oil & Gas Reporter*, Editor's Choice.

Holland, J.H. 1992. Genetic Algorithms. *Scientific American* **267** (1): 44-50.

Ilk, D., Stotts, G. W. J., Anderson, D. M., Mattar, L., and Blasingame, T.A. 2010. Production Data Analysis – Challenges, Pitfalls, Diagnostics. *SPE Reservoir Evaluation & Engineering* **13** (3): 538-552. SPE 102048-PA.

Javadpour, F., Fisher, D., Unsworth, M. 2007. Nanoscale Gas Flow in Shale Gas Sediments. *Journal of Canadian Petroleum Technology* **46**(10): 55-61.

Kim, J. U., Datta-Gupta, A., Brouwer, R. and Haynes, B.Jr. 2009. Calibration of High-Resolution Reservoir Models Using Transient Pressure Data. SPE 124834-MS.

Kulkarni, K. N., Datta-Gupta, A. and Vasco, D. W. 2000. A Streamline Approach for Integrating Transient Pressure Data into High Resolution Reservoir Models. SPE 65120-MS.

Landa, J. Kalia, P.K., Nakano, A., and Vashishta, P. 2005. History Match and Associated Forecast Uncertainty Analysis—Practical Approaches Using Cluster Computing. Paper IPTC 10751 presented at the SPE Annual Technical Conference and Exhibition, Denver, 5-8 October.

Lee, W. J. 1982. Well Testing. SPE Textbook Series. Richardson, Texas: Society of Petroleum Engineers.

Lee, W. J., Rollins, J. B. and Spivey, J. P. 2003. *Pressure Transient Testing*. SPE Textbook Series. Richardson, Texas: Society of Petroleum Engineers.

Ma, X.,Al-Harbi, M.,Datta-Gupta, A., and Efendiev, Y. 2008. An Efficient Two-stage Sampling Method for Uncertainty Quantification in History Matching Geological Models. *SPE Journal* **13** (1): 77-87. SPE 102476-PA.

Maxwell, S. C., Urbancic, T. I., Steinsberger, N., and Zinno, R. 2002. Microseismic Imaging of Hydraulic Fracture Complexity in the Barnett Shale. SPE 77440-MS.

Nordbotten J. M., Celia, M. A. and Bachu, S. 2004. Analytical Solutions For Leakage Rates Through Abandoned Wells. *Water Resources Research* **40**(4): W04204.

Oliver, D.S., Cunha, L.B., Reynolds, A.C. 1997. Markov chain Monte Carlo methods for conditioning a ppermeability field to pressure data. *Math Geol*. **29**(1), 61-91.

Oliver, D.S., Chen, Y. 2011. Recent Progress on Reservoir History Matching: A Review. *Comput Geosci* 15:185-221

Ouenes, A.,Bhagavan, S.,Bunge, P.H., and Travis, B.J. 1994. Application of Simulated Annealing and Other Global Optimization Methods to Reservoir Description: Myths and Realities. SPE 28415-MS.

Reynolds, A.C., He, N., Chu, L., Oliver, D.S. 1996. Reparameterization techniques for generating reservoir descriptions conditioned to variograms and well-test pressure data. SPEJ. **1**(4), 413-426. SPE 30588-PA.

Sambridge, M., and Mosegaard, K. 2002. Monte Carlo Methods in Geophysical Inverse Problems. *Reviews of Geophysics* **40** (3): 1009.

Sawyer, S.A.,Parsch, J.,Zhang, Z., and Hartl, D.L. 2007. Prevalence of positive selection among nearly neutral amino acid replacements in Drosophila. *Proceedings of the National Academy of Sciences of the United States of America* **104** (16): 6504-6510.

Schulze-Riegert, R.W., Axmann, J.K., Haase, O., Rian, D.T., and You, Y.L. 2002. Evolutionary Algorithms Applied to History Matching of Complex Reservoirs. SPE Reservoir Evaluation & Engineering **5**(2): 163-173. SPE 77301-PA.

Sethian, J. A. 1996. A Fast Marching Level Set Method for Monotonically Advancing Fronts. *Proceedings of the National Academy of Science* **93**: 1591-1595.

Sethian, J. A. 1999. Fast Marching Methods. *SIAM Review* **41**: 199-235.

Song B., Economides, M. J., and Ehlig-Economides, C. 2011. Design of Multiple Transverse Fracture Horizontal Wells in Shale Gas Reservoirs. SPE 140555-MS.

Sun, Y. and Fomel, S. 1998. Fast-marching Eikonal Solver in the Tetragonal Coordinates. Paper SEG 1998-1949 presented at the SEG Annual Meeting, New Orleans, Louisiana, 13-18 September.

Valko P. P. and Lee W. J. 2010. A Better Way To Forecast Production From Unconventional Gas Wells. SPE 134231-MS.

Vasco, D. W., Keers, and H., Karasaki, K. 2000. Estimation of Reservoir Properties Using Transient Pressure Data: An Asymptotic Approach. *Water Resour. Res.* **36**: 3447-3465.

Virieux, J., Flores-Luna, C., and Gibert, D. 1994. Asymtotic Theory for Diffusive Electromagnetic Imaging. *Geophysical Journal International* **119**: 857-868.

Weise T. 2008. Global Optimization Algorithms-Theory and Application. 3: 114. E-book at http://www.it-weise.de/

Williams, G.J.J., Mansfield, M., MacDonald, D.G., and D. Bush 2004. Top-Down Reservoir Modeling. SPE 89974-MS.

Winestock A. G. and Colpitts G. P. 1965. Advances in Estimating Gas Well Deliverability. *Journal of Canadian Petroleum Technology* 4 (3): 111-119

Xie, J., Gupta, N., King, M. J., and Datta-Gupta, A. 2012a, Depth of Investigation and Depletion Behavior in Unconventional Reservoir Using Fast Marching Methods, SPE 154532-MS.

Xie, J., Yang, C., Gupta, N., King, M. J., and Datta-Gupta, A. 2012b. Integration of Shale Gas Production Data and Microseismic for Fracture and Reservoir Properties Using Fast Marching Method. SPE 161357-MS.

Yang, P.H., Watson, A.T.1987. Automatic History-Matching with Variable-Metric Method. SPE 16977-MS.

Yin, J., Xie, J., Datta-Gupta, A. and Hill, A.D. 2011. Improved Characterization and Performance Assessment of Shale Gas Wells by Integrating Stimulated Reservoir Volume and Production Data. SPE 148969-MS.

Zafari, M., Reynolds, A.C., 2005. Assessing the Uncertainty in Reservoir Description and Performance Predictions With the Ensemble Kalman Filter. SPE 95750-MS.

Zhang, Y., Yang, C., King, M.J., and Datta-Gupta, A. 2013. Fast-Marching Methods for Complex Grids and Anisotropic Permeabilities: Application to Unconventional Reservoirs. SPE 163637-MS.

APPENDIX A

ASYMPTOTIC SOLUTION OF THE DIFFUSIVE EQUATION

The asymptotic method has been widely applied in various disciplines such as optical, medical and geophysical imaging (Virieux et al. 1994). We can take an analogy between a propagating pressure front and a propagating wave front since many concepts have their counterparts in petroleum engineering (Datta-Gupta and King. 2007). Vasco et al (2000) gives a high frequency asymptotic solution of the diffusivity equation for an impulse source or sink.

The transient pressure response in a heterogeneous permeable medium is governed by the diffusive equation,

$$\phi(\vec{x})\mu c_t \frac{\partial p(\vec{x},t)}{\partial t} = \nabla \cdot (k(\vec{x})\nabla p(\vec{x},t)) \quad \text{.....(A.1)}$$

In the above expression, we have spatially variable porosity $\phi(\vec{x})$, permeability $k(\vec{x})$, and constant fluid viscosity μ, total compressibility c_t. By applying a Fourier transform of Eq.(A.1), it can be expressed as the following in the frequency domain.

$$\phi(\vec{x})\mu c_t(-i\omega)\tilde{p}(\vec{x},\omega) = k(\vec{x})\nabla^2\tilde{p}(\vec{x},\omega) + \nabla k(\vec{x})\cdot\nabla\tilde{p}(\vec{x},\omega) \quad \text{.....(A.2)}$$

We can obtain an asymptotic solution for Eq. (A.2) if we consider a solution in terms of inverse powers of $\sqrt{-i\omega}$

$$\tilde{p}(\vec{x},\omega) = e^{-\sqrt{-i\omega}\cdot\tau(\vec{x})}\sum_{k=0}^{\infty}\frac{C_k(\vec{x})}{\left(\sqrt{-i\omega}\right)^k} \quad \text{.....(A.3)}$$

where, $\tau(\vec{x})$ is the propagation time of the pressure 'front', defined as 'diffusive time of flight', and $C_k(\vec{x})$ is the pressure amplitude at the k-th order.

The above expression of asymptotic solution is the sum of an infinite number of functions $C_k(\vec{x})$. Fortunately, the first few terms in the series can generally interpret important physical quantities. By substituting Eq.(A.3) into Eq.(A.2), we can obtain a new form with an infinite number of terms, and each term will contain $\sqrt{-i\omega}$ to some order. We may consider the sets of terms for any given order. If we consider the highest order in $\sqrt{-i\omega}$, those of order $\left(\sqrt{-i\omega}\right)^2$, we will obtain the expression corresponding to the propagation of a 'pressure front', which can be expressed as

$$i\omega\nabla\tau(\vec{x})\cdot\nabla\tau(\vec{x})C_0(\vec{x}) - i\omega\frac{\phi(\vec{x})\mu c_t}{k(\vec{x})}C_0(\vec{x}) = 0 \quad \text{.....(A.4)}$$

Assuming that $C_0(\vec{x})$ and ω are non-vanishing, we obtain

$$\sqrt{\alpha(\vec{x})}\cdot\left|\nabla\tau(\vec{x})\right| = 1 \quad \text{.....(A.5)}$$

where, $\alpha(\vec{x})$ stands for diffusivity and is defined as,

$$\alpha(\vec{x}) = \frac{k(\vec{x})}{\phi(\vec{x})\mu c_t} \quad \text{.....(A.6)}$$

Eq.(A.5) is in the form of widely known as Eikonal Equation. It suggests that the pressure 'front' propagates in the reservoir with a velocity given by the square root of diffusivity. The pressure 'front' propagation depends on reservoir and fluid properties, and independent of flow rate. Besides, the diffusive time of flight, $\tau(\vec{x})$ has unit of square root of time, which is consistent with scaling behavior of pressure diffusion.

APPENDIX B

DERIVATION OF EQUATIONS FOR HIGHLY COMPRESIBLE SHALE GAS FLOW

In this section, we show the details of derivations for the shale gas flow. Compared to water and oil, the specialty with high compressible gas flow is that properties, such as porosity, compressibility, and viscosity, are highly depends on pressure. The basic idea is express the pressure p and time t in the format of pseudo-pressure $m(p)$ and pseudo-time t_p respectively, and then re-derive all the flow equations in that pseudo format. We will discuss how to derive the diffusive equation, solve the diffusive equation in shale gas reservoir utilizing fast marching method, and derive the flow rate based on the drainage volume given by FMM.

B.1 Diffusive Equations

According to the conservation of mass, we have the governing equation given by Eq.(B.1).

$$\nabla \cdot (\rho \vec{v}) = -\phi(\vec{x}) \frac{\partial \rho}{\partial t} \quad \text{.....(B.1)}$$

Where, ρ , $\vec{v}$, $\phi(\vec{x})$ and indicate the density, velocity, and spatially variable porosity respectively. Combining the equation of state of gas, Eq.(B.2), and Darcy's law. Eq.(B.3), the Eq.(B.1) can be expressed as Eq.(B.4),

$$\rho = \frac{M}{RT}\left(\frac{p}{Z(p)}\right) \quad \text{.....(B.2)}$$

$$\vec{v} = -\frac{k(\vec{x})}{\mu(p)}\nabla p \quad \text{.....(B.3)}$$

$$\nabla \cdot \left[\frac{k(\vec{x})}{\mu(p)Z(p)}\, p\nabla p\right] = \phi \frac{\partial}{\partial t}\left[\frac{p}{Z(p)}\right] \quad \text{.....(B.4)}$$

where, M is the mass, R is the universal gas constant, T is the temperature, $Z(p)$ is the compressibility factor, $\mu(p)$ is viscosity, $k(\vec{x})$ is permeability.

$$c_t(p) = \frac{1}{\rho}\frac{d\rho}{dp} = \frac{Z(p)}{p}\frac{d}{dp}\left[\frac{p}{Z(p)}\right] \quad \text{.....(B.5)}$$

According to the definition of compressibility $c_t(p)$, Eq.(B.5), we can derive the formula in Eq.(B.6),

$$\frac{d}{d}\left[\frac{p}{Z(p)}\right] = \frac{c_t(p)p}{Z(p)}\frac{dp}{d} \quad \text{.....(B.6)}$$

$$m(p) = \left(\frac{\mu_g Z}{p}\right)_i \int_0^p \frac{pdp}{\mu_g Z} \quad \text{.....(B.7)}$$

$$t_p = \left(\mu_g c_t\right)_i \int_0^t \frac{dt}{\mu_g c_t} \quad \text{.....(B.8)}$$

If we take the pseudo-pressure $m(p)$ and pseudo-time t_p in the format of Eq.(B.7) and Eq.(B.8), and substitute them into Eq.(B.4), we can obtain the ultimate formula for the diffusive equation shown in Eq.(B.9).

$$\nabla \cdot \left[k(\vec{x}) \cdot \nabla m(\vec{x}, t_p)\right] = \phi(\vec{x}) \cdot \left[\mu(p) c_t(p)\right]_i \cdot \frac{\partial m(\vec{x}, t_p)}{\partial t_p} \quad \text{.....(B.9)}$$

B.2 Solution of Diffusive Equation

Similar to the derivation in Appendix A, by applying a Fourier transform of Eq.(B.9), it can be expressed as the following, Eq.(B.10), in the frequency domain

$$\phi(\vec{x}) \cdot \left[\mu(p) c_t(p)\right]_i \cdot (-i\omega) \tilde{m}(\vec{x}, \omega) = k(\vec{x}) \nabla^2 \tilde{m}(\vec{x}, \omega) + \nabla k(\vec{x}) \cdot \nabla \tilde{m}(\vec{x}, \omega) \quad \text{.....(B.10)}$$

We can obtain an asymptotic solution for Eq. (B.10) if we consider a solution in terms of inverse powers of $\sqrt{-i\omega}$

$$\tilde{m}(\vec{x}, \omega) = e^{-\sqrt{-i\omega} \cdot \tau(\vec{x})} \sum_{k=0}^{\infty} \frac{C_k(\vec{x})}{\left(\sqrt{-i\omega}\right)^k} \quad \text{.....(B.11)}$$

Follow the same derivation steps, we can obtain the Eikonal Equation shown in Eq.(B.12)

$$\sqrt{\alpha(\vec{x})} \cdot \left|\nabla \tau(\vec{x})\right| = 1 \quad \text{.....(B.12)}$$

where, $\alpha(\vec{x})$ stands for diffusivity and is defined as,

$$\alpha(\vec{x}) = \frac{k(\vec{x})}{\phi(\vec{x})\left[\mu(p) c_t(p)\right]_i} \quad \text{.....(B.13)}$$

The difference is that $\tau(\vec{x})$ describes the propagation front of the pseudo-pressure $m(p)$.

B.3 Expression for Gas Flow Rate

Based on the equation of state, shown in Eq.(B.2), we can obtain the transformation relationship of rate between reservoir condition and standard condition in Eq.(B.14)

$$q_{res} = q_g \cdot \frac{p_{sc}}{p} \cdot \frac{T}{T_{sc}} Z \quad \text{.....(B.14)}$$

$$q_{res} = \frac{kA}{\mu} \frac{\partial p}{\partial r} \quad \text{.....(B.15)}$$

The rate in reservoir condition can be given by Darcy's law, Eq.(B.15). Then the rate in standard condition can be expressed as in Eq.(B.16), where we combining the pseudo-pressure $m(p)$, Eq.(B.7), also.

$$q = \frac{T_{sc}}{T} \cdot \frac{p}{p_{sc}} \cdot \frac{kA}{\mu Z} \frac{\partial p}{\partial r} = kA \cdot \frac{T_{sc}}{T p_{sc}} \cdot \left(\frac{p}{\mu_g z} \right)_i \cdot \frac{\partial m(p)}{\partial r} \quad \text{.....(B.16)}$$

After obtaining the rate equation in Eq.(B.16), we found it's quite similar with the Eq.14 in Chapter 2. Just follow the same steps in Chapter 2, we can finally derive the rate equation based on the calculation of drainage volume shown in Eq.(B.17).

$$q_g(t_p) = \frac{T_{sc}}{T p_{sc}} \cdot \left(\frac{p}{\mu_g Z} \right)_i \cdot \frac{m(p_i) - m(p)}{\int_0^{V_p(t)} \frac{1}{k \cdot \phi \cdot A^2} (1 - \frac{V_p}{V_p(t_p)}) \cdot dV_p} \quad \text{.....(B.17)}$$

APPENDIX C

TRANSFORMATION FROM DIFFUSIVE TIME OF FLIGHT τ TO PHYSICAL TIME t

Through Eq.5 in Chapter 2, we can transform the entire diffusive time of flight field into real pressure front arrive time field by the geometric factor β related to flow pattern. Such as for linear flow, radial flow and spherical flow, the geometric factor β is 2, 4, and 6 respectively.

In a heterogeneous case, there is no global flow pattern anymore; quite often one flow regime is dominant during a certain time period, and then gradually changes to another flow regime. Thus, β should be understood in an averaged sense and is related to the geometry of the pressure front which can be of arbitrary shape and changing with time. This means we lost the exact meaning of the factor β. After verifying with well-known flow pattern, we propose the following formula to calculate the geometric factor β,

$$\beta(\tau) = 2\frac{d\ln V_p(\tau)}{d\ln \tau} \quad \text{.....(C.1)}$$

In the following, we run the cases for simple 1,2,3-dimensiton homogeneous reservoir. We present the relationship between the pore volume (drainage volume) and the diffusive time of flight τ in Fig.38-40 respectively, and the results show great agreement with Eq.(C.1). Summary and comparison is given in Table 5.

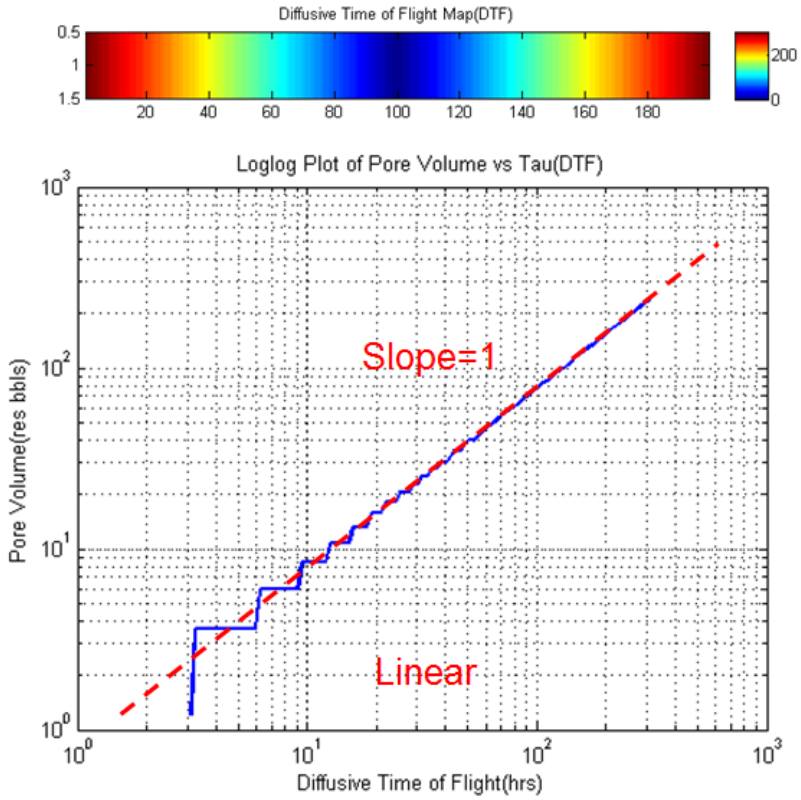

Fig.38 Relationship between pore volume and diffusive time of flight (1-dimension)

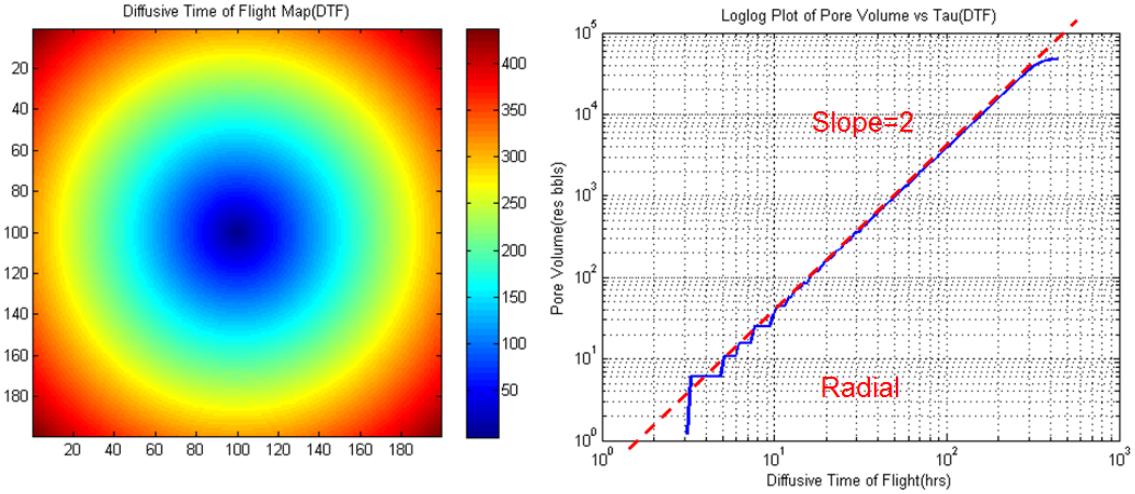

Fig.39 Relationship between pore volume and diffusive time of flight (2-dimension)

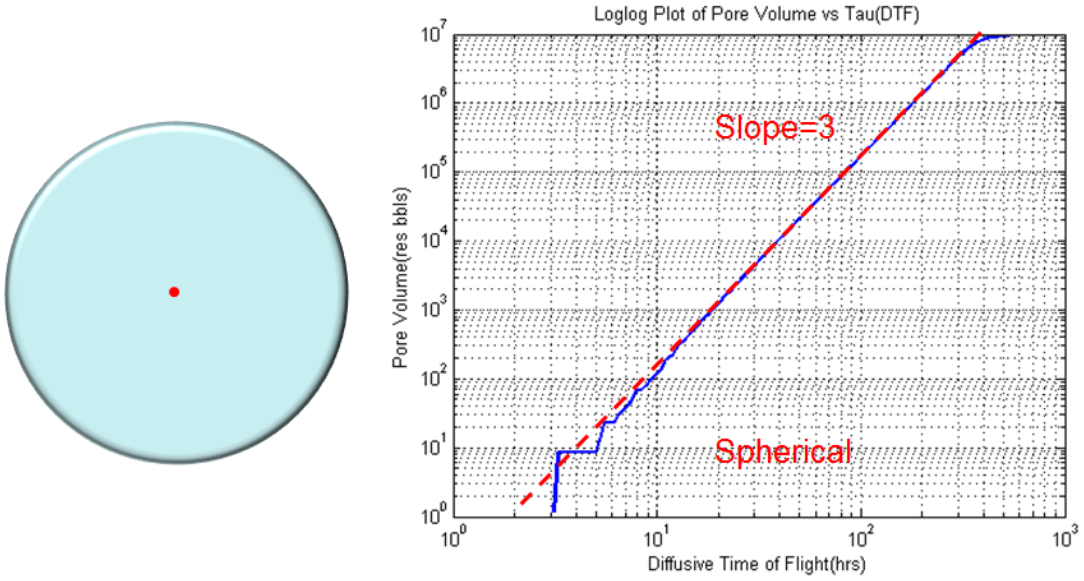

Fig.40 Relationship between pore volume and diffusive time of flight (3-dimension)

Table 5. The pore volume with diffusive time of flight for different flow regime

Flow Type	V_p	$V_p = f_n(\tau)$	**Slope in** $\log\log$ **Plot**	C_r
Linear	$2 \cdot r \cdot dy \cdot dz$	$2 \cdot \sqrt{\alpha} \cdot \tau \cdot dy \cdot dz$	1	2
Radial	$\pi \cdot r^2 \cdot h$	$\pi \cdot \alpha \cdot \tau^2 \cdot h$	2	4
Spherical	$4/3 \pi \cdot r^3$	$4/3 \pi \cdot \alpha^{1.5} \cdot \tau^3$	3	6

We also show a more complex synthetic model, which has two barriers in the middle, shown in Fig.41. This gives us a radial flow at the beginning, then linear flow, followed by approximate radial flow. Based on the proposed relationship in Eq.(C.1), the diffusive time of flight τ can be transformed to physical time t according to Eq.(C.2).

$$t = \left(\int_0^{\tau} \frac{d\tau'}{\sqrt{\beta(\tau')}} \right)^2 \quad \text{.....(C.2)}$$

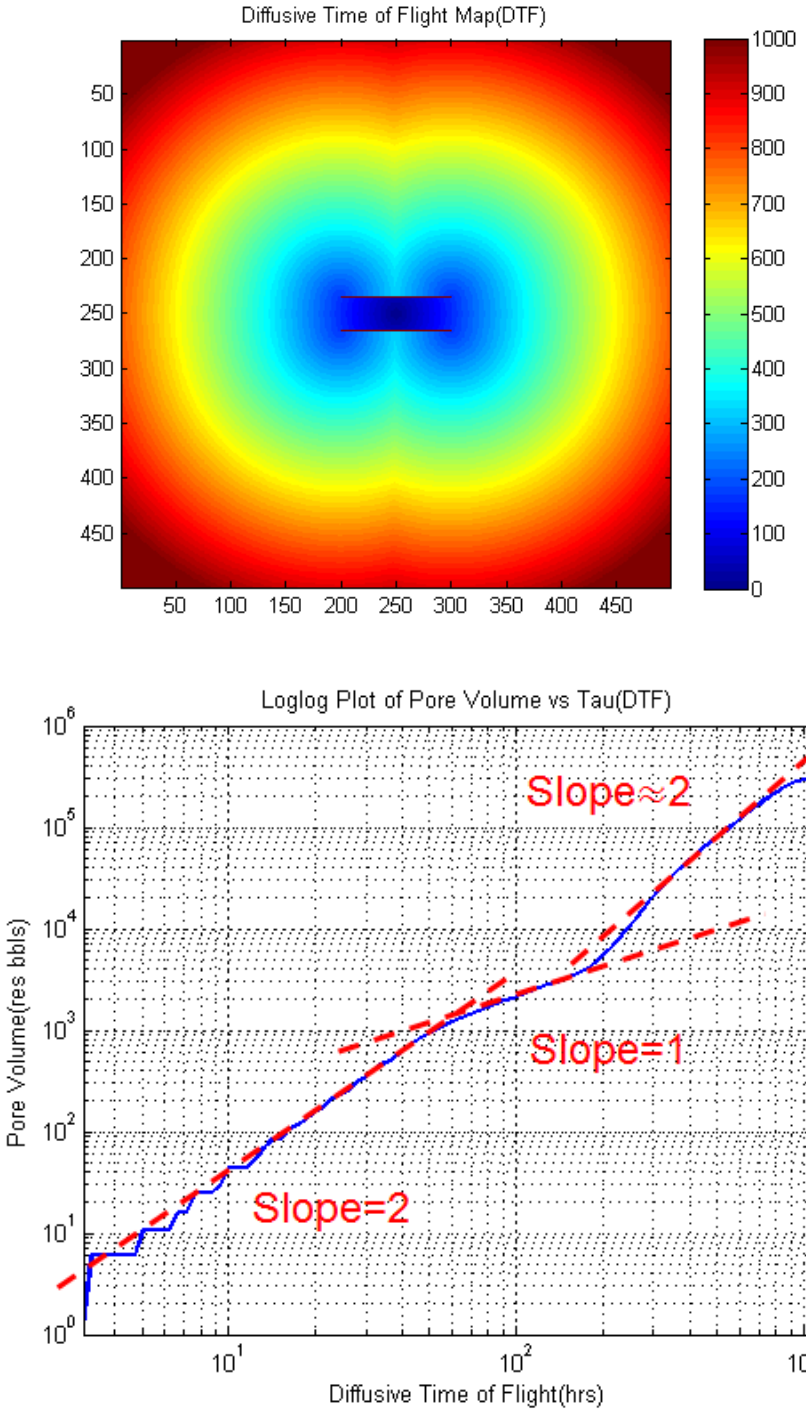

Fig.41 More complex synthetic model, a) diffusive time of flight map; b) relationship between pore volume and diffusive time of flight